Floquet Simulators for Topological Surface States in Isolation

Kun Woo Kim,[1,2,*] Dmitry Bagrets,[1] Tobias Micklitz,[3] and Alexander Altland[1]
[1]Institut für Theoretische Physik, Universität zu Köln, Zülpicher Straße 77, 50937 Köln, Germany
[2]Department of Physics, Chung-Ang University, 06974 Seoul, Republic of Korea
[3]Centro Brasileiro de Pesquisas Físicas, Rua Xavier Sigaud 150, 22290-180, Rio de Janeiro, Brazil

(Received 22 March 2022; accepted 28 November 2022; published 10 January 2023)

With recent advances in time-resolved device control, the dynamical engineering of novel quantum phases is becoming reality. One of the striking new options is the dynamical generation of space-synthetic dimensions, transcending the confines of static crystalline solid-state physics. We apply this principle to propose protocols allowing for the engineered realization of topological surface states in isolation. As a concrete example, we consider 3D topological surface states of a 4D quantum Hall insulator via a $(1+2_{\mathrm{syn}})$-dimensional protocol. We present first-principle analytical calculations demonstrating that no supporting 4D bulk phase is required for a 3D topological surface phase. We back the analytical approach by numerical simulations and present a detailed blueprint for the realization of the synthetic surface phase with existing quantum linear optical network device technology. We then discuss generalizations, including a proposal for a quantum simulator of the $(1+1_{\mathrm{syn}})$-dimensional surface of the common 3D topological insulator.

DOI: 10.1103/PhysRevX.13.011003

Subject Areas: Condensed Matter Physics, Mesoscopics, Topological Insulators

I. INTRODUCTION

Surface states of topological insulators (TI) define one of the most fascinating forms of quantum matter. Depending on their symmetries and dimensionality, they conduct charge, spin, or heat with topological protection against the detrimental effects of impurity scattering or interactions. These features make the TI surface distinct from any other form of quantum matter and are believed to harbor far-reaching potential applications in future devices. At the same time, our understanding of the TI surface physics remains incomplete, both experimentally and theoretically. For example, even in the absence of interactions, their conduction properties are not known quantitatively, and according to recent numerical work [1], they may even be enigmatic. The experimental analysis of surface transport is hindered by the inevitable presence of an "insulating" bulk, in quotation marks because heat or electric currents easily leak away from the surface hindering a clear separation of surface and bulk currents.

According to the bulk-boundary principle, no *lattice* quantum system in isolation can be in the universality class of the TI surface. The necessity of a supporting bulk follows from topological band theory or, more fundamentally, as a consequence of anomaly inflow. The main message of this paper is that this no-go theorem can be sidestepped within the wider framework of Floquet quantum matter. Specifically, we propose realizations of (dynamical) synthetic matter in universality classes indistinguishable from those of *isolated* (static) TI surfaces in the presence of effective disorder. Our work includes three novel conceptual elements: (i) the encoding of two- and three-dimensional surface-state topologies in multifrequency dynamical protocols, (ii) the first-principle demonstration of the equivalence between the quantum states engineered in this way and insulator surface states, and (iii) the formulation of a detailed experimental blueprint suggesting that this program can be implemented in realistic devices within the framework of current date technology.

Previous work [2,3] indeed pointed out the realizability of topological metallic phases in dynamically driven lattice systems. However, the presence of a lattice structure made these systems subject to the notorious fermion-doubling principle, which requires an even number of Dirac cones in the Floquet Brillouin zone. In the presence of impurities, these mutually gap out, spoiling the surface-state analogy. In order to realize a genuine surface state in isolation, a more radical departure from the solid-state crystal paradigm is required. In this paper, we demonstrate that the toolbox of quantum optics contains platforms that are up to this task: optical lattices [4,5] or linear optical networks [6–8] driven by multiple incommensurate

*Corresponding author.
kunx@cau.ac.kr

frequencies. The driving of d-dimensional realizations of such systems by d_{syn} incommensurate frequencies is microscopically identical to a time periodic (Floquet) dynamics acting in an effective system of dimensionality $d + d_{\mathrm{syn}}$ [9], where the structure of the Floquet operator in the d physical and d_{syn} synthetic dimensions depends on the driving protocol. Importantly, the correlations in the synthetic directions are not confined by the fermion-doubling theorem, and this will be key to the engineering of topological surface states in isolation. We label the $d + d_{\mathrm{syn}}$-dimensional Floquet metallic (FM) systems realized in this way as $\mathrm{FM}_{d+d_{\mathrm{syn}}}$ throughout the paper.

The simulation of higher-dimensional systems via driven low-dimensional physical platforms is experimental reality. In breakthrough experiments, it was applied to extend one-dimensional Anderson localization in the quantum kicked rotor [10–13] to higher dimensions. This process defined an effectively disordered FM_{1+2} and led to the first high-precision observation of a three-dimensional Anderson transition under parametrically controlled conditions [4,14].

However, the realization of the TI surface states addressed in this paper requires the additional structure of an internal bi-valued degree of freedom or "spin." (For earlier proposals to realize topological quantum matter with synthetic dimensions via the driving of systems with internal degrees of freedom, see Refs. [15,16].) Specifically, we need full control over the lattice nearest-neighbor hopping for a system with 2 internal degrees of freedom ("spin"). The required technology is not yet realized for the optical lattice [17], but it is available in the alternative platform of linear optical networks [18]. Therefore, we focus on this hardware and discuss the implementation of a $\mathrm{FM}_{1+1_{\mathrm{syn}}}$ and a $\mathrm{FM}_{1+2_{\mathrm{syn}}}$ TI surface state. We demonstrate by numerical control simulations that unique signatures of surface-state delocalization in the synthetic disordered system are observable for experimentally accessible timescales and length scales.

A further hallmark of our approach is that it realizes surfaces in effectively "disordered" phases lacking translational invariance. The reason for this is that the generation of synthetic dimensions requires noncommuting operators both in synthetic and physical space. The simultaneous presence of these operators in the dynamics leads to nonintegrability and chaotic fluctuations, physically equivalent to tunable disorder at mesoscopic length scales. Thus, our approach simulates the surfaces of disordered topological quantum matter, which one may take as an added element of realism.

The plan of the paper is as follows. In Sec. II, we present dynamical protocols of 1D quantum walks that utilize synthetic dimensions to simulate higher-dimensional systems. In Sec. III, we introduce a quantum simulator of topological insulator surface states in isolation using the example of the 4D quantum Hall insulator. We introduce a 1D quantum-walk protocol, discuss its topological property, and report on numerical simulations of the protocol, all supporting the idea that the surface states of the 4D quantum Hall insulator can be simulated by the 1D quantum walk. We then discuss a concrete blueprint, realizing the quantum walk within the existing optical linear network setup. Section IV provides further details and discusses generalizations. Specifically, we introduce a simulator of surface states of a 3D quantum spin Hall insulator. We conclude in Sec. VI. Aiming to keep the presentation as nontechnical as possible, the details of various derivations are relegated to the appendixes.

II. DYNAMICAL PROTOCOLS

Consider the quantum walk of a spin-1/2 particle on a 1D lattice, generated by successive applications of translations and spin rotations. The single time-step evolution operator is of the general form

$$\hat{U}_t = \sum_m \hat{R}_m(t) \otimes \hat{T}_m, \tag{1}$$

where $\hat{T}_m$ shifts the walker by m lattice sites, and $\hat{R}_m(t) = \vec{r}_m(t) \cdot \vec{\sigma}$ rotates its spin. Here and in the following, $\vec{\sigma} = (\sigma_0, i\boldsymbol{\sigma})$ and $\vec{r}_m = (r_{m0}, \boldsymbol{r}_m)$ are four-component vectors such that $\sigma_0 = \mathbb{1}_2$, $\boldsymbol{\sigma} = (\sigma_x, \sigma_y, \sigma_z)$, and $\vec{r}_m \in \mathbb{C}^4$. Central for our proposal is the time-dependent spin-rotation axes $r_m(t)$, which are dynamically changed in the course of the walk. As we show below, using dynamical protocols with periods that are incommensurate with the discrete time step of the evolution operator Eq. (1) enables the simulation of dynamics in higher-dimensional systems. In the following, we focus on quantum walks with short-range hops to the nearest neighbors, $m \in \{0, -1, +1\}$. The unitary operator Eq. (1) then simplifies to

$$\hat{U}_t = \vec{r}_0 \cdot \vec{\sigma} + (\vec{r}_+ \cdot \vec{\sigma}) \otimes \hat{T}_+ + (\vec{r}_- \cdot \vec{\sigma}) \otimes \hat{T}_-, \tag{2}$$

and unitarity sets the following constraint on $\vec{r}_0$, $\vec{r}_\pm$: Expressing $\vec{r}_\pm = \vec{r}_r \pm i\vec{r}_i$, with $\vec{r}_{r,i} \in \mathbb{R}^4$ real four-component vectors, the latter are orthogonal, $\vec{r}_r \cdot \vec{r}_i = 0$, $\vec{r}_0 \cdot \vec{r}_{r,i} = 0$, and equal in magnitude, $|\vec{r}_r| = |\vec{r}_i| = \frac{1}{2}\sqrt{1 - |\vec{r}_0|^2}$ at each time step t (see Appendix A for details).

Finally, we add spin-dependent spatial disorder to the dynamics. To this end, we introduce the unitary matrix $(\hat{U}_{\mathrm{dis}})_{nn'} = \hat{U}_{\mathrm{dis}}(n)\delta_{nn'}$, where $\hat{U}_{\mathrm{dis}}(n)$ are independent random spin-rotation matrices, acting locally on each site n. The single time-step evolution $|\psi_t\rangle = \mathcal{U}_{t,t-1}|\psi_{t-1}\rangle$ generating the 1D quantum walk is then composed of the combined operator,

$$\mathcal{U}_{t,t-1} = \hat{U}_t \hat{U}_{\mathrm{dis}}, \tag{3}$$

and we next discuss its potential to simulate higher-dimensional dynamics.

A. Synthetic dimensions from multifrequency dynamical protocols

Let us specify the protocol in Eq. (1) to rotations $\hat{R}_m$, which depend on $d_{\rm syn}$ time-dependent functions,

$$\hat{R}_m(t) \equiv \hat{R}_m(\varphi_{2,t}, \ldots \varphi_{d_{\rm syn}+1,t}), \tag{4}$$

and where the time dependence for each of the functions is of the form $\varphi_{i,t} = k_i + \omega_i t$ with frequencies $\omega_2, \ldots, \omega_{d_{\rm syn}+1}$ incommensurate to 2π and among themselves. Furthermore, $k_{\rm syn} \equiv (k_2, \ldots, k_{d_{\rm syn}+1})$ are arbitrary initial phases that we consider to be averaged over in our dynamical protocols below. The mapping to an effectively $1 + d_{\rm syn}$-dimensional Floquet system is achieved by extending the Hilbert space of the system and interpreting these phases as momenta conjugate to integer-valued coordinates $n_{\rm syn} = (n_2, \ldots, n_{d_{\rm syn}+1})$, with canonical commutation relations $[\hat{n}_i, \hat{k}_j] = -i\delta_{ij}$ between the corresponding operators. We note that $\hat{n}_i = -i\partial_{k_i}$ in the phase-momentum representation of the theory. These coordinates extend the lattice in $1 + d_{\rm syn}$ dimensions with sites $\mathbf{n} = (n_1, n_{\rm syn})$, where $n_1 = n$ is the physical lattice coordinate, conjugate to a phase k_1. In the same notation, $\mathbf{k} = (k_1, k_{\rm syn})$.

Using the general relation $e^{ia\hat{n}} f(\hat{k}) e^{-ia\hat{n}} = f(\hat{k} + a)$, the time dependence in the arguments of the rotation operator can be removed by the gauge transformation

$$\hat{R}_m(t) = e^{i\omega_j t\hat{n}_j} R_m(0) e^{-i\omega_j t\hat{n}_j}, \tag{5}$$

where a summation over $j = 2, \ldots, 1 + d_{\rm syn}$ is implicit. This enables us to express the time-evolution operator $\mathcal{U}_{t,0} \equiv \prod_{\tau=0}^{t-1} \mathcal{U}_{\tau+1,\tau}$ as

$$\begin{aligned} |\psi_t\rangle &= \mathcal{U}_{t,t-1}\mathcal{U}_{t-1,t-2}\cdots\mathcal{U}_{1,0}|\psi_0\rangle \\ &= e^{i\omega_j t\hat{n}_j}[\mathcal{U}_{0,-1}e^{-i\omega_j\hat{n}_j}]^t|\psi_0\rangle. \end{aligned} \tag{6}$$

We notice that the time evolution is governed by powers of the single Floquet operator $\mathcal{U}_F \equiv \mathcal{U}_{0,-1}e^{-i\omega_j\hat{n}_j} = \hat{U}_{t=0}\hat{U}_{\rm dis}e^{-i\omega_j\hat{n}_j} \equiv U_{\mathbf{k}}W_{\mathbf{n}}$. Here, $\hat{W}_{\mathbf{n}} \equiv \hat{U}_{\rm dis}(n_1)e^{-i\omega_j\hat{n}_j}$ is diagonal in the coordinate representation while $\hat{U}_{\mathbf{k}} = \hat{U}_0(\mathbf{k})$ is momentum diagonal. To understand this last statement, we note that in Eq. (1) the coordinate translation operator $\hat{T}_m f(n_1) = f(n_1 - m)$ affords the representation $\hat{T}_m = e^{im\hat{k}_1}$ while $\hat{R}_m(0)$ depends on the phases $k_{\rm syn}$.

To summarize, our dynamics is governed by the effective multidimensional Floquet operator $\mathcal{U}_F = \hat{U}_{\mathbf{k}}\hat{W}_{\mathbf{n}}$ factoring into two pieces, which are individually diagonal in coordinates and momenta, respectively. Our numerical simulations below demonstrate that the combined action of these operators induces integrability breaking, physically equivalent to static disorder, in all $1 + d_{\rm syn}$ dimensions. However, before introducing quantum simulators for the combined effects of disorder and topology in this setting, we briefly introduce observables probing topological surface states in an experimentally accessible way.

B. Observable

The spreading after t time steps of a wave packet, describing a quantum walker initially prepared at site $n_1 = 0$ with spin σ, can be expressed as

$$\langle \Delta X^2 \rangle \equiv \sum_{n_1}\sum_{\sigma',\sigma} n_1^2 \overline{|\langle n_1, \sigma'|\mathcal{U}_{t,0}|0,\sigma\rangle|^2}. \tag{7}$$

Here, the sum is over spin orientations $\sigma = \uparrow, \downarrow$, and $\overline{(\ldots)}$ refers to the average over both an ensemble of realizations of the random rotations $\hat{U}_{\rm dis}$ and the initial momenta $k_{\rm syn}$. In a mixed coordinate-momentum representation, basis states of the extended Hilbert space are defined by the kets $|n_1, \sigma\rangle \to |n_1, k_{\rm syn}, \sigma\rangle$. Specifically, the initial state of the quantum walker is confined to $n_1 = 0$ and independent of synthetic momenta. Upon Fourier transformation to a full coordinate representation, $|n_1, k_{\rm syn}, \sigma\rangle \to |n_1, n_{\rm syn}, \sigma\rangle \equiv |\mathbf{n}, \sigma\rangle$, this translates to localization at $|\mathbf{0}, \sigma\rangle$ in both physical and synthetic space. The spreading of the quantum walker is thus given by (see further details in Appendix B)

$$\langle \Delta X^2 \rangle \equiv \sum_{\mathbf{n}}\sum_{\sigma',\sigma} n_1^2 \overline{|\langle \mathbf{n}, \sigma'|\mathcal{U}_F^t|\mathbf{0},\sigma\rangle|^2}. \tag{8}$$

The correlation function Eq. (8) describes the width in the physical n_1 direction of the wave packet initially prepared at $n_1 = 0$, and its finite time scaling encodes information on the quantum-walk dynamics.

C. Topological invariants

All of our topological FMs discussed below are characterized by integer-valued invariants. These numbers afford two different interpretations:

1. Topological invariants and FM classification

The first relates to a classification of FM phases in terms of the periodic table of Hamiltonian insulators [3]. Its idea is to map the translation-invariant part of the Floquet operator $U_{\mathbf{k}}$ onto a block off-diagonal "auxiliary" Hamiltonian

$$H_{\mathbf{k}} = \begin{pmatrix} & U_{\mathbf{k}} \\ U_{\mathbf{k}}^\dagger & \end{pmatrix}. \tag{9}$$

This Hamiltonian inherits the symmetries of $U_{\mathbf{k}}$ but, in addition, possesses a "chiral" symmetry due to its

off-diagonality; it belongs to a symmetry class that is different from the class of the Floquet theory. For example, if the latter is in class A (just unitary), H will be in class AIII (chiral, no further symmetries). Bott periodicity then implies that a class-A Floquet theory realizes a FM state in odd effective dimension $D = d + d_{\mathrm{syn}}$ if the associated D-dimensional Hamiltonian in class AIII is also topologically nontrivial. Furthermore, the presence of topologically nontrivial phases of the Hamiltonian theory is signaled by invariants mathematically identical to those constructible for the Floquet theory. For example, in the above case, these invariants are "winding numbers" defined by a unitary map from odd-dimensional Brillouin zones $\mathbf{k} \mapsto U_{\mathbf{k}}$ into the unitary group. These winding numbers classify class-AIII insulating phases in odd dimensions and class-A Floquet metallic phases in even dimensions.

2. Topological invariants and localization theory

To understand this statement in more concrete terms, we note that our Floquet theories are categorically disordered or chaotic. Their physical description requires real-space methods, as defined by the nonlinear σ models of disordered conductors. In these theories, protection against the effects of Anderson localization, i.e., topological metallicity, is introduced via topological terms [see Eq. (25) for a concrete example]. These terms take a physical effect provided their coupling constants are not vanishing. Below, we demonstrate in two concrete case studies that the momentum-space invariants responsible for the "abstract" classification of topological FMs indeed appear as coupling constants in topological field theories. In this way, they serve a double function in the classification and the localization theory of FMs. In the latter context, they protect topological FMs from developing a "mobility gap" and force them to remain metallic, including FMs in low dimensions, which would otherwise show strong localization.

III. THREE-DIMENSIONAL TOPOLOGICAL FLOQUET METAL $\mathrm{FM}_{1+2_{\mathrm{syn}}}$

The concept of synthetic dimensions is general and can be realized for a wide class of driven or kicked Floquet systems [16,19–22]. In the following, we introduce a specific realization in $1 + 2_{\mathrm{syn}}$ dimensions, physically equivalent to the surface of a four-dimensional topological insulator in symmetry class A (aka a "four-dimensional quantum Hall insulator").

A. Model

We consider a one-dimensional quantum walker, whose forward and backward hopping amplitudes are time-dependent matrices coupling to the internal degrees of freedom (see Fig. 1). In the notation of the previous section, its time evolution from one discrete time step t to the next is defined through

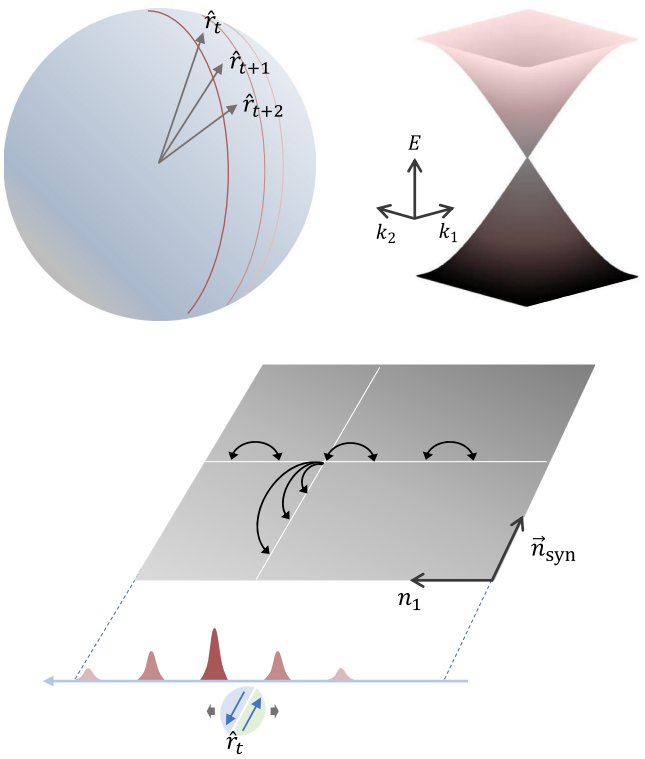

FIG. 1. A 1D quantum walk with time-dependent spin quantization axis $\hat{r}_t$ simulating dynamics of a 2D systems when the period of r_t is incommensurate with the discrete time steps of the evolution operator. This engineering of synthetic dimensions allows us to sidestep the fermion-doubling principle and to simulate, e.g., the 2D surface states in isolation of a 3D quantum spin Hall insulator.

$$\hat{U}_t = \frac{1}{2}(\sigma_0 + \mathbf{r}_t \cdot \boldsymbol{\sigma}) \otimes \hat{T}_+ + \frac{1}{2}(\sigma_0 - \mathbf{r}_t \cdot \boldsymbol{\sigma}) \otimes \hat{T}_-, \tag{10}$$

where the specific choice

$$\mathbf{r}_t = (\cos\varphi_{2,t} \sin\varphi_{3,t}, \sin\varphi_{2,t} |\sin\varphi_{3,t}|, \cos\varphi_{3,t}), \tag{11}$$

will be explained momentarily, and the time dependence of the phase arguments is defined below Eq. (4). Turning to the gauge-equivalent representation in terms of a Floquet operator acting in a space with one physical and two synthetic dimensions, we describe the dynamics through the Floquet operator $\hat{\mathcal{U}}_F = \hat{U}_{\mathbf{k}} \hat{W}_{\mathbf{n}}$ with $U_{\mathbf{k}} = U_{t=0}$ and $\hat{T}_\pm = e^{\pm i k_1}$. For later reference, we note that the unitary $U_{\mathbf{k}}$ affords different representations, each useful in its own right. First, it is straightforward to verify that

$$\begin{aligned} \hat{U}_{\mathbf{k}} &= \exp\left[i k_1 (\mathbf{r}(\mathbf{k}) \cdot \boldsymbol{\sigma})\right], \\ \mathbf{r}(k) &= (\cos k_2 \sin k_3, \sin k_2 |\sin k_3|, \cos k_3). \end{aligned} \tag{12}$$

Alternatively, we may represent the spin matrices as rotations acting upon a translation operator with z-axis

polarization: $\hat{U}_{\mathbf{k}} = R_3(-k_2')R_2(-k_3)\hat{T}_C R_2(k_3)R_3(k_2')$, with $\hat{T}_C = e^{ik_1\sigma_3}$, the momentum $k_2' = k_2 \mathrm{sgn} k_3$, and spin-rotation operators $R_j(\varphi_l) = \exp(i\varphi_l\sigma_j/2)$.

A crucial feature of this realization is its nonanalytic dependence on the momentum variables through $|\sin k_3|$. In the Fourier conjugate representation, it translates to long-ranged hopping $(\mathcal{U}_F)_{n_3 n_3'} \sim |n_3 - n_3'|^{-2}$ [23]. At this point, the synthetic dimensions begin to play an essential role: Power-law hopping in physical dimensions is difficult to engineer. More importantly, the $|\sin k_3|$ nonanalyticity is the essential resource allowing us to sidestep the fermion-doubling theorem and to realize a synthetic topological metal.

1. Winding number

To elucidate this last point, we interpret Eq. (12) as a mapping from the 3D Brillouin zone torus to the two-dimensional special unitary group $\mathbb{T}^3 \to \mathrm{SU}(2)$ (with unit determinant, $\det[U_{\mathbf{k}}] = 1$) and assign the topological invariant

$$W = \frac{1}{24\pi^2}\int d^3\mathbf{k}\epsilon^{\mu\nu\rho}\mathrm{tr}[(U_{\mathbf{k}}^\dagger\partial_\mu U_{\mathbf{k}})(U_{\mathbf{k}}^\dagger\partial_\nu U_{\mathbf{k}})(U_{\mathbf{k}}^\dagger\partial_\rho U_{\mathbf{k}})] = \frac{1}{2\pi^2}\int d^3\mathbf{k}\sin^2 k_1|\sin k_3| = 4, \tag{13}$$

where $\mu,\nu,\rho \in \{1,2,3\}$. As anticipated above, it is the nonanalyticity $|\sin k_3|$ that leads to a nonvanishing winding number. Conversely, a model with analytic k dependence would necessarily lead to a vanishing winding number, in accordance with the fermion-doubling theorem.

Driving protocols with nonanalytic functions, simulating power-law hoppings in synthetic space, allow us to construct Floquet operators with even winding numbers $W \in 2\mathbb{Z}$: The starting points of our construction are realizations of unitary operators, which display finite winding numbers over certain subsets of a Brillouin zone, say, $W = n$ in region I and $W = -n$ in region II. (The numbers must add to zero by virtue of the fermion-doubling theorem.) Then, the trick to generate a finite winding number is to modify the momentum dependence in region II via a sign change in the momentum dependence, which inverts the winding number to $W|_{\mathrm{II}} = +n$ and $W = 2n$ in total. We also construct an alternative model with the minimal winding possible in this scheme, $W = 2$. However, since it is rather involved, we opted for a discussion of the simpler $W = 4$ variant, Eqs. (10) and (11). We also emphasize that winding numbers for topological Floquet systems cannot be simply understood from their low-energy effective Hamiltonians [24]. Note that $W = 4$ of Eq. (12) is not, e.g., related to four Weyl cones in a low-energy description, but rather, it stores information on the entire Brillouin zone [see also discussion on dispersion of Eq. (12) in the next subsection].

The invariant in Eq. (13) indicates topological metallicity of our Floquet system. Within the alternative interpretation discussed above, the nonvanishing winding number W signals topological nontriviality of the "auxiliary" class-A III Hamiltonian. Bott periodicity implies nontrivial phases of 4D class-A systems (the four-dimensional quantum Hall effect), and the original Floquet system describes the physics of its three-dimensional metallic surface state. In more concrete terms, we will see in Sec. V that the winding number W appears as a building block in our construction of a gapless effective field theory equivalent to that of a three-dimensional topological metal.

B. Numerical simulations

To independently verify the topological metallic nature of the 3D dynamics simulated by the protocol in Eq. (10), we run the numerical simulations. More specifically, we simulate the quantum walk with trivial and nontrivial winding numbers for varying effective disorder strengths by introducing additional bandwidths in the model, as we discuss next. This allows us to test our main prediction, that is, the absence of Anderson localization for all disorder strength for finite windings W, contrasting Anderson localization at large disorder for vanishing winding number $W = 0$.

1. Simulation details

We numerically study the time evolution of initially localized wave packets, under the influence of the 1D quantum-walk operator in Eq. (10). To allow for a comparison of topologically trivial and nontrivial quantum walks with the same energy-momentum dispersion relation of the clean system, we implement the walk with $|\sin\varphi_{3,t}|$, as indicated in Eq. (12), and a second protocol with $|\sin\varphi_{3,t}|$ replaced by $\sin\varphi_{3,t}$. A metal-to-insulator transition with increasing disorder strength is expected for the second protocol. The static spatial disorder $\hat{U}_{\mathrm{dis}}$ is implemented by randomly drawing spin-rotation matrices from the uniform Haar measure. In other words, the disorder strength is fixed, and we need to introduce some tunable parameter, allowing us to drive a (possible) metal-to-insulator transition. We then notice that Eq. (12) and its topologically trivial cousin have no energy dispersion in the $k_{2,3}$ direction, which makes the latter always prone to localization. At the same time, we can perturb the original models to generate a dispersion with tunable bandwidth w in the $k_{2,3}$ direction. This then allows us to study a delocalization transition as a function of w. To realize this idea, we multiply the original single time-step evolution operators by the unitary operator

$$\hat{U}_w = \exp[iw(\sin k_{2,t}\sigma_1 + \sin k_{3,t}\sigma_2)]. \tag{14}$$

We then study the time scaling of the average spread $\langle\Delta X^2\rangle$ of the initial wave packet in the physical dimension.

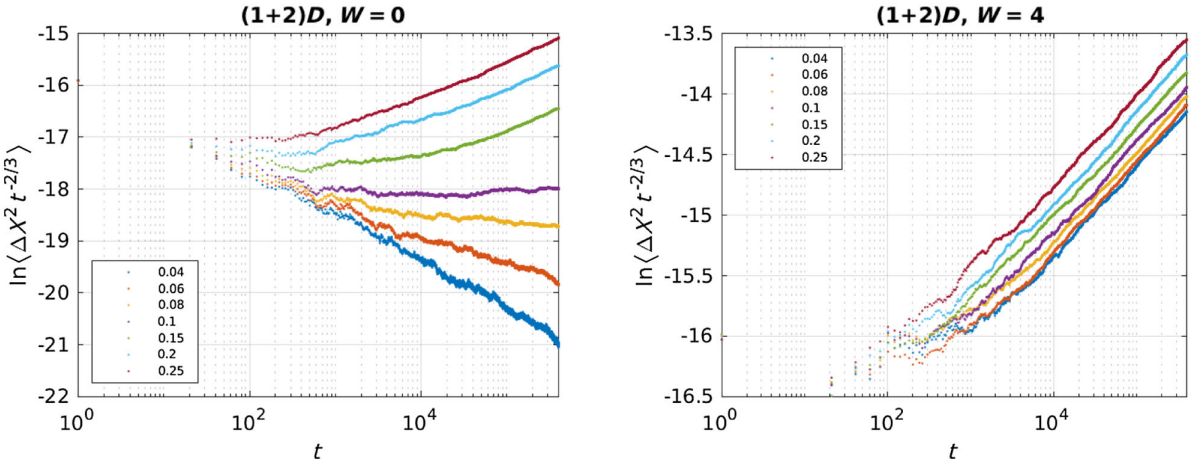

FIG. 2. Spread of the quantum walker as a function of time steps for the two protocols and different values of bandwidth w introduced in Eq. (14). To facilitate observation of the metal-to-insulator transition, the width of the wave packet is rescaled by the critical scaling at the transition, $\langle \Delta X^2 \rangle \sim t^{2/3}$. Left panel: topologically trivial protocol, $W = 0$, which shows a metal-to-insulator transition for $w \simeq 0.1$. Right panel: topological nontrivial variant, $W = 4$, which shows no signatures of localization, i.e., $\langle \Delta X^2 \rangle \sim t$ for all values of w and up to $t \sim 5 \times 10^5$ time steps.

2. Results

Figure 2 shows the time evolution of $\langle \Delta X^2 \rangle$ for the two protocols and different values of the bandwidth w, as indicated in the legend. The vertical axis is rescaled by the time dependence $\langle \Delta X^2 \rangle \sim t^{2/3}$ expected at the metal-to-insulator transition [5]. For the trivial protocol $W = 0$ (left panel), one clearly sees the metallic ($w > 0.1$) and insulating ($w < 0.1$) regimes separated by critical scaling at $w \simeq 0.1$. In contrast, the topological nontrivial protocol with $W = 4$ (right panel) shows metallic behavior for all values of w, with $\langle \Delta X^2 \rangle \sim t$ up to the largest time steps 5×10^5. The two incommensurate frequencies here are chosen as $\omega_2 = 2.4\sqrt{5}$, $\omega_3 = 2.4\sqrt{15}$, and disorder averaging is over 50 realizations for each data point. We also notice that the long-time numerical results are independent of the specific value for the incommensurate frequencies.

In the case of the trivial protocol $W = 0$, deviations from classical scaling $\langle \Delta X^2 \rangle \sim t$ signal Anderson localization, and eventually the dynamics will entirely freeze, $\langle \Delta X^2 \rangle \sim t^0$, on longer timescales and length scales. The important observation for us is that a clear distinction between quantum simulators of trivial and topological metallic phases is noticeable already for a small number of $\mathcal{O}(20)$ time steps [see Figs. 3(c) and 3(d)]. This is crucial for an experimental implementation of the quantum walks, as we discuss next.

C. Experimental realization: A $\mathrm{FM}_{1+2_{\mathrm{syn}}}$ simulator

So far, we have shown how the freedom of choosing operators of arbitrary k dependence in the synthetic momentum space allows for the engineering of topological Floquet operators that cannot exist in autonomous lattice environments. Specifically, we have (i) proposed a concrete dynamical protocol based on a 1D quantum walk, (ii) shown that this simulates a topological metal, e.g., realized on the isolated surface of a 4D quantum Hall insulator, and (iii) demonstrated that its most characteristic feature—absence of Anderson localization at strong disorder—can be observed already after $\mathcal{O}(20)$ time steps. The final piece of our proposal is to indicate an experimental platform that offers the required flexibility to implement dynamical protocols for spin-1/2 walkers. Here, we argue that linear optical networks are ideally suited to realize the proposed quantum simulators. After a brief review of their principal elements, we suggest a blueprint for the quantum Hall simulator.

1. Principle elements

In the typical optical realization of a quantum walk, photons propagate through a network of linear elements—viz. beam splitters, phase shifters, and polarization plates—realizing the "step" and "coin" operations. The step operation typically implements chiral hopping (here as a matrix in spin space)

$$\hat{T}_{\mathcal{C}} \equiv \begin{pmatrix} \hat{T}_+ & \\ & \hat{T}_- \end{pmatrix}, \tag{15}$$

translating the walker to the right (T_+) or left (T_-) according to its spin being in the up (first component) or down state (second component), respectively. The dynamical coin operations realize spin rotations $\hat{R}(t)$. Using a Euler angle decomposition, they can be generated

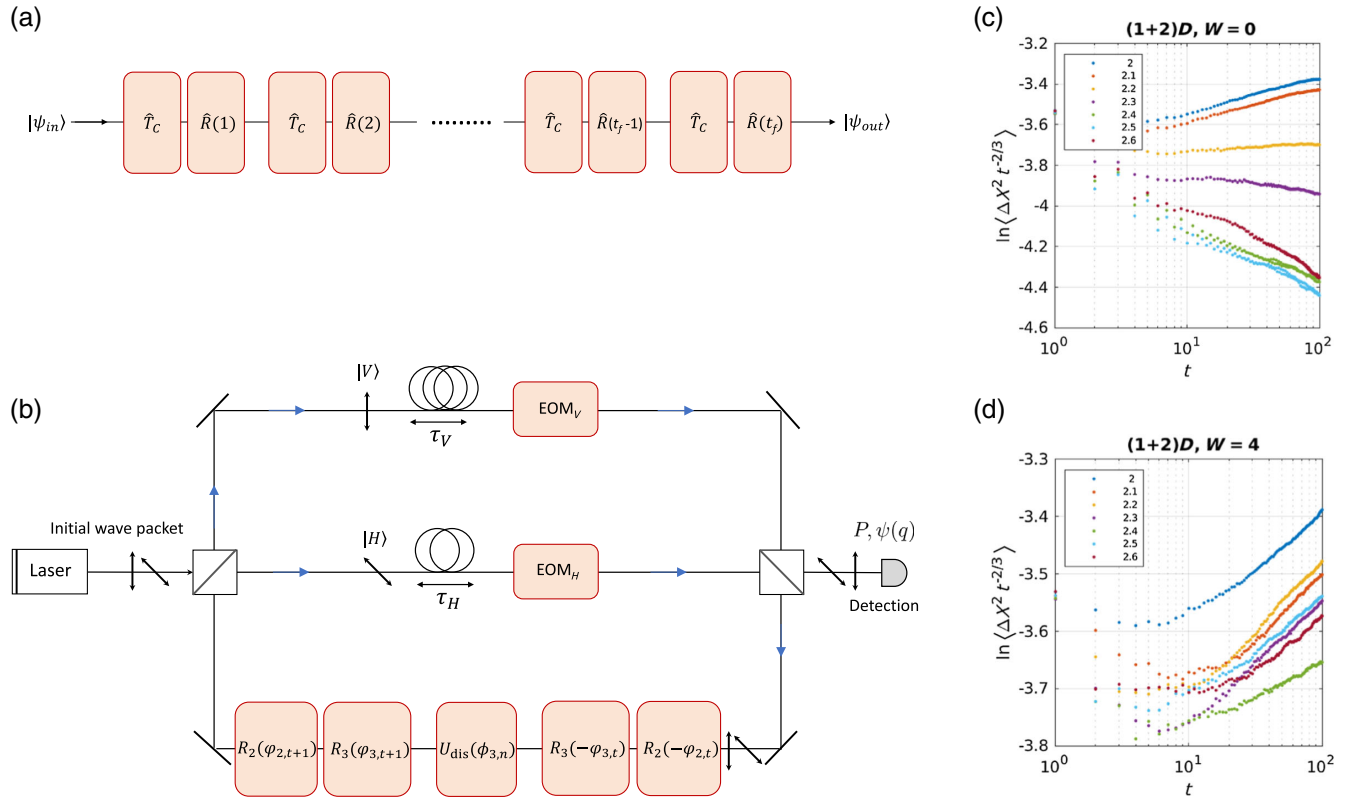

FIG. 3. (a,b) Blueprint of an optical linear network simulating the topological surface states of a 4D quantum Hall insulator in the quantum-walk setting. The feedback loop is built of the step operator $\hat{T}_C$ (upper and middle arms) followed by the coin operator $\hat{R}(t) = R_{t+1}\hat{U}_{\rm dis}R_t^\dagger$ (lower arm)—for details, see main text. To the left and right of the loop, source and detection units are connected. The source consists of a laser and a polarizing beam splitter (PBS), allowing for the preparation of the initial state. The passage to the detection unit can be activated by the dynamically tunable EOMs following the fiber lines of the step operation. In the detection unit, photons are registered by an avalanche photodiode (APD). (c,d) Numerical simulations of wave-packet spreading for trivial and topological quantum walks, here for varying incommensurate frequencies. The latter are chosen as $\omega_2 = C\sqrt{5}$ and $\omega_3 = C\sqrt{15}$ for several values $2.0 \le C \le 2.6$ (see legends). Differences between the two systems become visible already after $t \gtrsim 10$ time steps: The topological metal (d) shows robust diffusion for all values of C, while a crossover from diffusive to subdiffusive dynamics is observed as $C > 2.4$ for the trivial metal (c).

from repeated application of elementary rotations around any two of the three internal axes,

$$\hat{R}_j(\varphi_{l,t}) = \exp\left(i\varphi_{l,t}\sigma_j/2\right), \qquad j = y, z, \quad l = 2, 3, \quad (16)$$

with Pauli matrices operating in spin space. The great flexibility offered by optical linear networks is that Euler angles $\varphi_{l,t} = k_l + \omega_l t$ can be changed dynamically during the realization of the quantum walk.

The successive application of chiral step and coin operations composing the quantum-walk protocol is implemented in a "feedback loop" [see Fig. 3(b)]. Typically, a coherent laser pulse attenuated to an average single photon per pulse injects photons into the linear network. Horizontal and vertical polarizations of the photon constitute the internal "spin" states. The step operation $\hat{T}_C$ is realized in time, employing a polarizing beam splitter in combination with fiber delay lines. In other words, horizontally and vertically polarized photons are separated by the beam splitter and sent through fiber lines of different lengths. The length mismatch of the fibers introduces a well-defined delay between the two polarization components. When coherently recombined, the temporal separation of the two components is equivalent to the spatial separation by two lattice sites induced by the chiral translation to left and right neighbors of the 1D lattice. Dynamical coin operations $\hat{R}_j(\varphi_{l,t})$ are realized via tunable polarization rotations. In practice, the dynamical control over only one rotation axis—e.g., the z axis—is required, and rotations around the remaining axes are realized by the combination with suitable polarization controllers, i.e., half- and quarter-wave plates [25].

The dynamical control is achieved via control voltages applied to fast-switching electro-optic modulators (EOMs) that change rotation angles on timescales shorter than a step operation. Recent progress allows us to operate the latter

without high additional losses, and walks up to $t = 30$–40 time steps have been reported within this setup (see, e.g., Refs. [8,18]). From the numerical simulations of the previous section, we expect this to be sufficient to distinguish the dynamics of a topological metal from a trivial Floquet metal. After the light pulses have been fed back into the loop of step and coin operations, realizing a single time-step operation, for the desired number of time steps, they are released to the detection unit [see Fig. 3(b)]. Repeating the procedure for varying numbers of time steps and different realizations of coin operations, one obtains the walker's probability distribution, which allows for the full characterization of its dynamics.

2. *Blueprint for the* $\mathbf{FM}_{1+2_{\mathrm{syn}}}$

A detailed blueprint for an optical linear network simulating the topological $\mathrm{FM}_{1+2_{\mathrm{syn}}}$ is shown in Fig. 3. A crucial observation here is that the chiral translational U_t in Eq. (10) with tunable spin-quantization axis $\mathbf{r}_t$ can be implemented via a step operation $T_{\mathcal{C}}$ dressed by coin operations, $\hat{U}_t = \hat{R}_t^\dagger \hat{T}_{\mathcal{C}} \hat{R}_t$, with the coin matrix $\hat{R}_t$ being a product of two elementary rotations, $\hat{R}_t = \hat{R}_y(\varphi_{3,t})\hat{R}_z(\varphi_{2,t})$, where

$$\varphi_{3,t} = k_3 + \omega_3 t, \tag{17}$$

$$\varphi_{2,t} = \begin{cases} k_2 + \omega_2 t & \sin(\varphi_{3,t}) \geq 0, \\ -k_2 - \omega_2 t & \sin(\varphi_{3,t}) < 0 \end{cases} \tag{18}$$

[note the conditional value of $\varphi_{2,t}$ depending on the sign of $\sin(\varphi_{3,t})$, which follows from the definition (11) of the vector $\mathbf{r}_t$]. The role of $\hat{R}_t$ is to rotate the $\mathbf{z}$ axis into the instantaneous spin quantization axis $\mathbf{r}_t$.

In the linear network setup, it is convenient to start the feedback loop with a step operation. Thus, reorganizing spin rotations and the local disorder potential in the originally defined one-step evolution operator $\mathcal{U}_{t,t-1} = \hat{U}_t \hat{U}_{\mathrm{dis}}$ (with $\hat{U}_{\mathrm{dis}}$ specified below), we construct the equivalent one as the following succession of step and coin operations:

$$\mathcal{U}_{t+1,t} = \hat{R}(t)\hat{T}_{\mathcal{C}}, \qquad \hat{R}(t) = \hat{R}_{t+1}\hat{U}_{\mathrm{dis}}\hat{R}_t^\dagger. \tag{19}$$

This sequence is then iterated for the desired number of time steps.

Figure 3(a) schematically shows the elements of quantum-walk operations to be applied to an initial localized wave packet before the detection after t_f time steps. The actual implementation of the linear optical network can be prepared as in Fig. 3(b), realizing chiral quantum-walk and coin operators. The $\mathrm{EOM}_{V,H}$ are equipped for the initiation and the readout of the quantum-walk simulation. For the static disorder in real space, we suggest following the protocol used in the numerical simulations with fixed bandwidth. In other words, we choose $\hat{U}_{\mathrm{dis}} = R_z(\phi_{n_1})$ with static local angles ϕ_{n_1}, randomly drawn from the unit circle $-\pi \leq \phi_{n_1} < \pi$, and frequencies ω_2, ω_3 indicated in the previous section.

Figures 3(c) and 3(d) show numerical results for the quantum simulators of the trivial ($W = 0$) and topological ($W = 4$) metals over a range of experimentally accessible time steps. Here, the bandwidth is set to $w = 0$, and incommensurate frequencies are varied as $\omega_2 = C\sqrt{5}$ and $\omega_3 = C\sqrt{15}$, with values of C indicated in the legend. There are already notable differences between the two systems after $t \gtrsim 10$ time steps: Dynamics for the topological metal is diffusive for all values of C, while the trivial system shows a C-dependent behavior reminiscent of a metal-insulator transition as C is increased. Notice, however, that the metallic behavior for small values $C = 2$ and 2.1 only holds for a short time, and localization sets in at longer times (i.e., for the trivial protocol, there is no true metallic phase at $w = 0$, as discussed above).

This finalizes our discussion of a quantum simulator for the surface states of a 4D quantum Hall insulator. Next, we discuss generalizations to other dimensions and symmetry classes.

IV. TWO-DIMENSIONAL FLOQUET TOPOLOGICAL METAL $\mathbf{FM}_{1+1_{\mathrm{syn}}}$

To illustrate the generality of our approach, we discuss the example of a quantum simulator for surface states in a symmetry class different from the quantum Hall insulators. Specifically, we propose a simulator for the 2D surface states of a class-AII quantum spin Hall insulator in $d = 3$.

To this end, we start from a 1D quantum walk, Eq. (2), with a dynamical protocol,

$$\begin{aligned} \vec{r}_0 &= \frac{1}{2}(1 - \cos\varphi_{2,t}, 0, 0, \sin\varphi_{2,t}), \\ \vec{r}_r &= \frac{1}{4}(-1 - \cos\varphi_{2,t}, 0, 0, \sin\varphi_{2,t}), \\ \vec{r}_i &= \frac{1}{4}(0, |\sin\varphi_{2,t}|, -1 - \cos\varphi_{2,t}, 0), \end{aligned} \tag{20}$$

where $\varphi_{2,t} = k_2 + \omega_2 t$ and the frequency ω_2 is incommensurate to 2π. The three vectors in Eq. (20) are orthogonal to each other, and unitarity of the single time-step evolution operator follows from $|\vec{r}_0| = |\sin\varphi_{2,t}/2|$ and $|\vec{r}_{r,i}| = \frac{1}{2}|\cos\varphi_{2,t}/2|$ (see also Appendix A). Upon Fourier transformation in the physical coordinate and gauge transformation to eliminate time dependence of the driving protocol, we arrive at the Floquet operator

$$\hat{U}_{\mathbf{k}} = (\hat{r}_0 \cdot \vec{\sigma}) + (\vec{r}_+ \cdot \vec{\sigma})e^{ik_1} + (\vec{r}_- \cdot \vec{\sigma})e^{-ik_1}, \tag{21}$$

where $k_2 = \varphi_{2,t=0}$ and $\vec{r}_\pm = (\vec{r}_r \pm i\vec{r}_i)$. We notice that the specific choice of the driving protocol leads to the

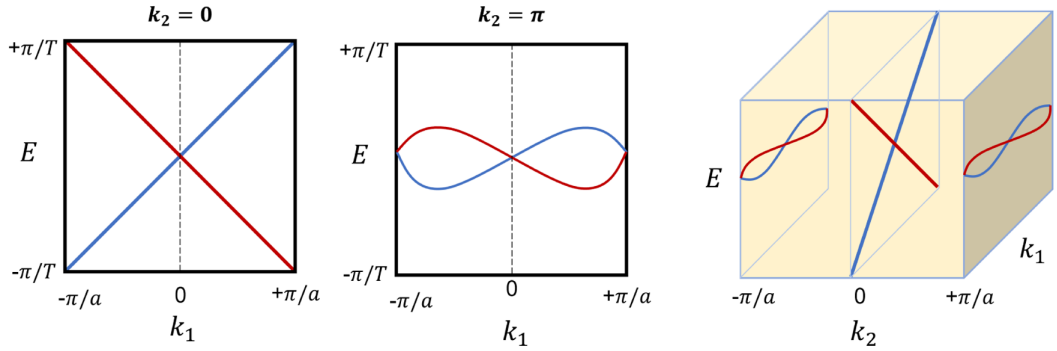

FIG. 4. Dispersion relations of the quasienergy spectrum of the two-band model along the high-symmetry lines $k_2 = 0$ (left panel) and $k_2 = \pi$ (middle panel), respectively (see also discussion in the main text). The former contributes to the topological invariant by the factor $\mathrm{Pf}[w_{\mathbf{\Lambda}_1}]\mathrm{Pf}[w_{\mathbf{\Lambda}_2}] = -1$, while the latter gives the factor $\mathrm{Pf}[w_{\mathbf{\Lambda}_3}]\mathrm{Pf}[w_{\mathbf{\Lambda}_4}] = 1$. Here, $w_{\mathbf{k}}$ is the antisymmetric sewing matrix. Right panel: visualization of dispersions along the high-symmetry lines in the 2D Brillouin zone.

nonanalytical n_2 component proportional to $|\sin k_2|$. It is again this unusual dependence, impossible to realize on a lattice with finite range hopping, that allows us to sidestep the fermion-doubling theorem. It is readily verified that Eq. (21) satisfies the time-reversal relation $\sigma_2 \hat{U}_{\mathbf{k}}^T \sigma_2 = \hat{U}_{-\mathbf{k}}$ of class-AII systems. These systems host topological insulating $\mathbb{Z}_2$ phases in 3D and thus topological metallic Floquet phases in 2D.

A. Topological invariant

To demonstrate the topological nature of the protocol in Eq. (20), we focus on the translational-invariant part $U_{\mathbf{k}}$ and consider the latter as a map from the 2D Brillouin zone torus to the special unitary group $\mathbb{T}^2 \to \mathrm{SU}(2)$ ($\det[\hat{U}_{\mathbf{k}}] = 1$). Time-reversal symmetry imposes that $n(\mathbf{k}) \| e_0$ at the four time-reversal-invariant momenta: $\mathbf{\Lambda}_1 = (0,0)$, $\mathbf{\Lambda}_2 = (0,\pi)$, $\mathbf{\Lambda}_3 = (\pi,0)$, and $\mathbf{\Lambda}_4 = (\pi,\pi)$. At these points, the so-called sewing matrix $w_{\mathbf{k}} = -i\sigma_2 \hat{U}_{\mathbf{k}}^T$ is antisymmetric, and the map $\hat{U}_{\mathbf{k}}$ is thus characterized by the $\mathbb{Z}_2$ topological index,

$$W_{\mathbb{Z}_2} = \prod_{i=1}^{4} \mathrm{Pf}[-i\sigma_2 \hat{U}_{\mathbf{\Lambda}_i}^T] = -1, \tag{22}$$

where, in the last identity, we used that $\hat{U}_{\mathbf{\Lambda}_1} = \sigma_0$ for Eq. (21) while $\hat{U}_{\mathbf{\Lambda}_i} = -\sigma_0$ for $i = 2, 3, 4$. Notice that the nontriviality of the index follows from the specific choice of the n_2 component.

Building on the alternative interpretation of the topological invariant discussed earlier, $W_{\mathbb{Z}_2}$ signals topological nontriviality of its auxiliary class-DIII Hamiltonian [3]. Indeed, time-reversal symmetry of the latter is inherited from the Floquet operator, while the block off-diagonal structure induces the additional chiral structure. In this interpretation, Eq. (22) then encodes topological properties of the class-DIII system in 2D [26].

For a more intuitive interpretation of Eq. (22), we prove in Appendix D that the Pfaffians can be expressed as $\mathrm{Pf}(w_{\mathbf{\Lambda}_j}) = -\exp(i\epsilon_{\mathbf{\Lambda}_j})$, where $\epsilon_{\mathbf{\Lambda}_j}$ are the quasienergies of $U_{\mathbf{k}}$ at the time-reversal-invariant momenta $\mathbf{\Lambda}_j$. The $\mathbb{Z}_2$ topological invariant thus affords the alternative representation

$$W_{\mathbb{Z}_2} = \exp\left(i \sum_{j=1}^{4} \epsilon_{\Lambda_j}\right), \tag{23}$$

which has a simple intuitive visualization. To this end, consider the 1D dispersion relations $E_{\pm}^0(k_1) = \epsilon_{\pm}(k_1, k_2 = 0)$ and $E_{\pm}^{\pi}(k_1) = \epsilon_{\pm}(k_1, k_2 = \pi)$ of the quasienergy spectrum $\epsilon_{\pm}(\mathbf{k})$ of the two-band model along the two high-symmetry lines $k_2 = 0, \pi$, respectively. As shown in Fig. 4, bands $E_{\pm}^0(k_1)$ touch at $\mathbf{\Lambda}_1$ and are split by energy 2π at $\mathbf{\Lambda}_2$. Bands $E_{\pm}^{\pi}(k_1)$, on the other hand, touch at both momenta $\mathbf{\Lambda}_3$ and $\mathbf{\Lambda}_4$. This different pattern of the dispersion along the two high-symmetry lines results in the negative topological index $W_{\mathbb{Z}_2} = -1$, as formalized by Eq. (23).

B. Numerical simulations

We simulate the time evolution of an initially localized wave packet in $(1 + 1_{\mathrm{syn}})$ dimensions for three different Floquet operators (all involving maximal disorder in the real coordinate, viz. random Haar unitaries): The first operator simulates the topological Floquet metal, described in Eq. (20). Sharing the low-energy physics of 2D class-AII topological metallic surface states, we expect anomalous superdiffusion, $\langle \Delta X^2 \rangle \sim t \ln t$ [27], which is confirmed in the left panel of Fig. 5. Numerical calculations are performed for the incommensurate frequency $\omega_2 = \sqrt{5}C$ (where the value C is indicated in the legend), and each data point is obtained from averaging over 50 disorder realizations. The second Floquet operator simulates a critical state in class A. In other words, replacing the nonanalytic function in Eq. (20) by an analytic function,

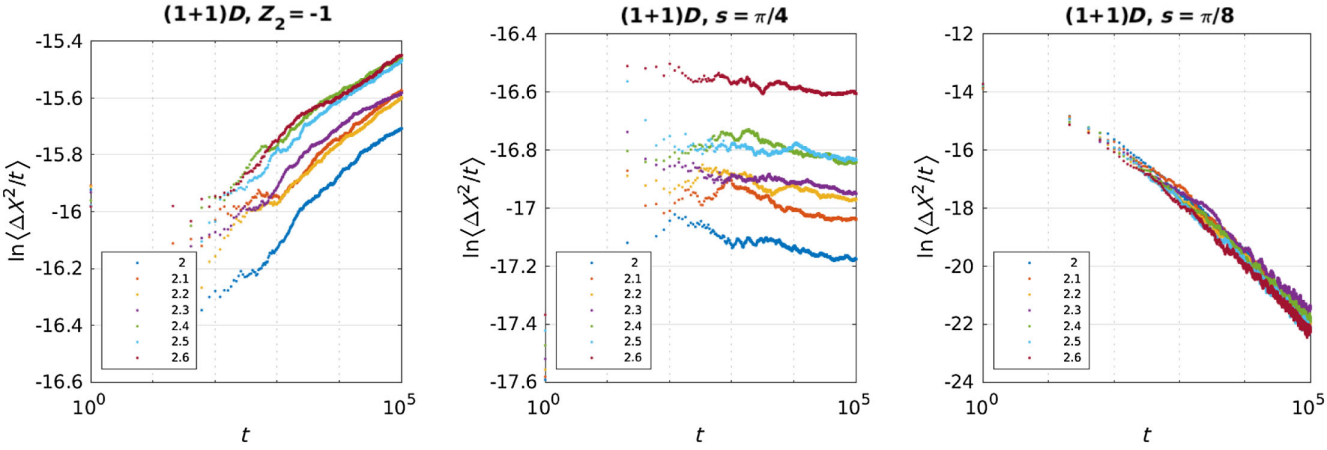

FIG. 5. Scaled width of a wave packet $\langle \Delta X^2/t \rangle$ for different quantum walks in $(1+1_{\mathrm{syn}})$D and monitored over 5×10^5 time steps. Left panel: topological quantum walk showing anomalous superdiffusion. Middle panel: critical quantum walk of a class-A model fine-tuned to a topological phase transition. Right panel: topologically trivial quantum walk subject to Anderson localization. Colors correspond to incommensurate frequencies $\omega_2 = \sqrt{5}C$, with values C indicated in the legend.

$|\sin\varphi_{2,t}| \to \sin\varphi_{2,t}$, we obtain a $(1+1_{\mathrm{syn}})$-dimensional class-A model fine-tuned to a quantum critical point separating two topologically distinct Anderson insulating phases [28]. The presence of a topological θ term fine-tuned to the angle $\theta = \pi$ in this case protects against Anderson localization. The middle panel of Fig. 5 indeed indicates subdiffusion on all accessible timescales in our numerics. Notice that the energy dispersions for the first and second Floquet operators are identical, and differences in the dynamics therefore are rooted in the different topological terms. For the third Floquet operator, we tune the second Floquet operator away from the quantum critical point. The low-energy physics in this case has a θ term, however, with topological angle θ detuned from the critical value (see also next section). At long distances or times, we then expect conventional Anderson insulating behavior, which is confirmed in the right panel of Fig. 5.

C. Incommensurability and synthetic dimensions

So far, we have discussed idealized quantum-walk protocols with irrational driving frequencies and frequency ratios. However, in view of our proposed experimental implementations, a comment on rational approximations is in order. A driving frequency $\omega = 2\pi(p/q)$ generates a synthetic dimension of finite extension around q. If the dynamics on length scales less than or around q is diffusive, a dimensional crossover takes place on timescales comparable to the diffusion time associated with distance scales around q. On larger scales, the system behaves as if it existed in one dimension lower. The precision by which frequencies have to be chosen thus depends on the experimentally probed timescales: The above crossover should remain invisible in that it occurs on scales larger than the above crossover scales. (The precise value of these scales depends on system-specific parameters, notably the effective diffusion constant.)

To make these general considerations more quantitative, we numerically study the protocol for the $\mathrm{FM}_{1+1_{\mathrm{syn}}}$ of the previous section, substituting $\omega_2 = 2.6\sqrt{5}$ by $\omega_2 = 2\pi\alpha$ with rational approximations of increasing periodicity $\alpha = 0.9,\ 0.92,\ 0.925,\ 0.9253$. The left panel of Fig. 6 shows the width of a wave packet normalized by the width expected for diffusive dynamics, $\Delta X^2/t$, as a function of t on a log-log scale. At the crossover scale to one-dimensional dynamics, the (approximately) constant profile for diffusive dynamics turns into a linear slope,

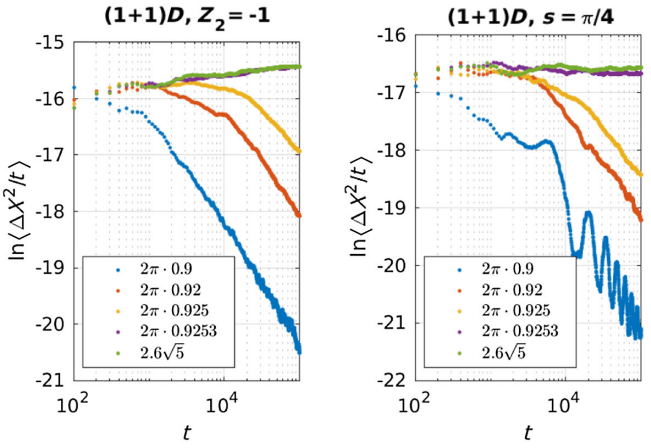

FIG. 6. Wave-packet spread for quantum simulators of finite-size class-AII topological metals $\mathrm{FM}_{1+1_{\mathrm{syn}}}$ (left panel) and 2D class-A critical metals (right panel). The size of the compact dimension increases with the number of decimals kept in the rational approximation α, and the dimensional crossover in the dynamics is observed at increasingly later times (see also discussion in main text).

characteristic of localized wave packets. As anticipated, the characteristic timescale increases with the periodicity of the rational approximation, i.e., the number of decimals kept in α. The right panel of Fig. 6 shows the corresponding numerical results for the 2D critical class-A metal, also discussed in the previous section.

V. LOW-ENERGY PHYSICS

A. Class A

To support our claim that the protocol in Eq. (10) simulates the isolated surface of a topological 4D quantum Hall insulator, we next apply field-theory methods for disordered systems. Our aim in this section is to show that the low-energy physics of both systems is described by the same effective field theory. Readers interested in more background material on field theories of disordered systems are invited to look into the Supplemental Material [29].

To begin, let us recall that the dispersion of the low-energy excitations simulated by the clean contribution to the Floquet operator (10) is linear in k_1 and flat in all other directions. The emergence of Weyl fermions at low energies then results from the interplay of a nontrivial topology and nonintegrable chaotic fluctuations induced by the protocol. Indeed, we see that the presence and stability of the Weyl fermions are topologically protected by the winding number, precisely in the same manner as the four Weyl cones of surface states in a 4D class-A insulator at the $\nu = 4$ integer quantum Hall plateau.

Applying methods for disordered systems [30–35], we can evaluate correlation functions for the dynamical quantum walk defined by Eq. (10) in the effective quantum-field-theory (QFT) framework. Its matrix degree of freedom T acts in a replica space supplemented by additional causal ("retarded" and "advanced") structure. Within such QFT, the physics at long timescales and length scales is described by an effective action $S[T] = S_\sigma[T] + S_{\text{top}}[T]$, consisting of two contributions:

$$S_\sigma = \frac{1}{8}\sum_{i,j=1}^{3} \sigma_{ij}^{(0)} \text{Tr}(\partial_i Q \partial_j Q), \tag{24}$$

$$S_{\text{top}} = iW \times S_{\text{CS}}[T]. \tag{25}$$

Here, the winding number W is defined in Eq. (13), with U the translational-invariant part of the Floquet operator. The matrix field $Q = TQ_0T^{-1}$ is expressed as rotations around $Q_0 \equiv \sigma_3 \otimes \mathbb{1}_R$ with the Pauli matrix σ_3 operating in the causal sector of the $2R$-dimensional vector space, and $\text{Tr} = \int d^3x \text{tr}$ involves the trace over the latter and 3D space of physical and synthetical dimensions. Readers interested in further details are invited to look into the Supplemental Material [29], where we explain the mathematical structures and outline a derivation of the above action. Here, we restrict ourselves to a discussion of the physical implications of Eqs. (24) and (25).

The first observation is that S_σ is the standard model for Anderson localization in disordered single-particle systems, here in 3D. For sufficiently strong disorder, viz. sufficiently small "bare" values $\sigma_{ij}^{(0)}$, the model flows to an Anderson insulating fixed point at long length scales with vanishing coupling constant. Here, we consider Haar random disorder, for which

$$\sigma_{ij}^{(0)} = \frac{1}{2}\int d^3\mathbf{k} \text{tr}(\partial_{k_i} U_{\mathbf{k}} \partial_{k_j} U_{\mathbf{k}}^{-1}) \tag{26}$$

is purely determined by the translational-invariant part of the Floquet operator. As we detailed above, we can then drive a metal-to-insulator transition by tuning the bandwidth of the system; see discussion around Eq. (14).

The Anderson delocalization scenario at strong disorder is provided by the second topological term with Chern-Simons action S_{CS},

$$S_{\text{CS}} = \frac{1}{8\pi}\sum_{s=\pm} s \text{Tr}\left(A_s \wedge dA_s + \frac{2}{3} A_s \wedge A_s \wedge A_s\right). \tag{27}$$

Here, $A_s = T^{-1}dTP^s$, where $P^s = \frac{1}{2}(1 + s\sigma_3) \otimes \mathbb{1}_R$ are projectors onto the retarded ($s = +$) and advanced ($s = -$) sectors of the $2R$-dimensional vector space. The key observation then is that the combined action defined by Eqs. (24) and (25) realizes a 3D topological metal, which, unlike systems with $W = 0$, has a conductance growing in system size even at strong disorder. In the field-theory language, this means that the "bare" coupling $\sigma_{ij}^{(0)}$ grows under renormalization, and correlation functions show similar behavior. The same action, $S[T] = S_\sigma[T] + S_{\text{top}}[T]$, has previously been identified as describing (at length scales exceeding the mean free path) W disordered Weyl cones realized on the surface of a 4D class-A quantum Hall insulator surface [36,37]. We have thus established the equivalence between the protocol in Eq. (10) for driven synthetic matter and quantum Hall insulator surface states, demonstrating that both belong to the same universality class.

B. Class AII

The nontrivial $\mathbb{Z}_2$ index in Eq. (22) indicates that the low-energy physics of the dynamical protocol in Eq. (20) is dominated by a single Weyl fermion, similar to the isolated surface of a 3D quantum spin Hall insulator. The single Weyl cone is not immediate from the low-energy dispersion of the clean Floquet operator in Eq. (20) but rather emerges as a consequence of the nontrivial topology in combination with the chaotic fluctuations induced by the protocol.

Applying field-theory methods of disordered systems, we can again derive a low-energy effective theory

$S[T] = S_\sigma[T] + S_{\text{top}}[T]$ that allows for the calculation of correlation functions at long timescales and length scales. Here, S_σ is the σ model action, already introduced in Eq. (24), now for the 2D system in the symplectic class AII. The latter alone predicts a metal-to-insulator transition for strong disorder, a scenario changed by the second topological contribution

$$S_{\text{top}} = i\frac{\theta}{\pi} \times \Gamma[g]|_{g(0,\mathbf{x})=Q(\mathbf{x})}. \tag{28}$$

Here, $\theta = \pi W_{\mathbb{Z}_2}[U]$ is the topological angle from Eq. (22), and

$$\Gamma[Q] = \frac{1}{24\pi}\int_{\mathcal{M}} \text{tr}(\Phi_g \wedge \Phi_g \wedge \Phi_g) \tag{29}$$

is "half" of a Wess-Zumino-Witten (WZW) action, involving the usual deformation of the field degree of freedom T. Specifically, $\Phi_g \equiv g^{-1}dg$ with $g(x_0 = 0, \mathbf{x}) = Q(\mathbf{x})$, and integration is over half the 3-torus $\mathcal{M} = [0,1] \times [-1,1]^2$. This topological action was previously identified [38,39] for the description of the 3D disordered quantum Hall insulator. We refer the interested reader to the accompanying Supplemental Material [29] for further explanations; here, we only focus on a discussion of the physical implications, which are similar to those of the Chern-Simons action encountered in the unitary class. For $\theta = \pi$, the system flows to a conformally invariant quantum critical point, where the coupling constant of S_σ assumes a disorder independent value [Eq. (26)], implying the absence of Anderson localization also for strong disorder. The same principle of delocalization is at work on 2D surfaces of 3D topological spin quantum Hall insulators. The latter are indeed described by the same effective action [38,40], and we have thus shown that the protocol in Eq. (20) belongs to the same universality class as the isolated surface of a quantum spin Hall insulator.

C. More on topological terms

The possibility for disordered systems to escape the fate of Anderson localization is signaled by topological terms in their low-energy field-theory description. Whether the latter are allowed depends on the dimension of the system and the target space of the field degree of freedom. The effective action of the aforementioned 3D class-A system contains a Chern-Simons action, with a coupling constant that is the winding number of the Floquet operator. The winding number and Chern-Simons action signal the presence of topologically inequivalent classes of mappings

$$U_{\mathbf{k}}: \mathbb{T}^3 \mapsto \text{SU}(2), \tag{30}$$

$$Q(x_0, \mathbf{x}): \mathbb{T}^{(3+1)} \mapsto \text{U}(2R)/[\text{U}(R) \times \text{U}(R)]. \tag{31}$$

Here, the boundary configuration $Q(x_0 = 0, \mathbf{x})$ is parametrized by the 3D field $T(\mathbf{x})$, used in the Chern-Simons action in Eq. (27). Introducing the deformation parameter $0 \le x_0 \le 1$, continuously transforming the boundary value $Q(x_0 = 0, \mathbf{x})$ to the constant matrix $Q(x_0 = 1, \mathbf{x}) = \sigma_3 \otimes \mathbb{1}_R$, the Chern-Simons action can be expressed as a WZW term. The latter is precisely what is necessary for a 3D class-A system to avoid Anderson localization (see Supplemental Material [29]). The winding number of $U_{\mathbf{k}}$ given in Eq. (13), on the other hand, defines the coupling constant of the WZW term. In other words, the combination of nontrivial homotopy groups $\pi_3(\text{SU}(2)) = \mathbb{Z}$ and $\pi_4(\text{U}(2R)/[\text{U}(R) \times \text{U}(R)]) = \mathbb{Z}$ allows for nonvanishing coupling constants weighting topologically nontrivial field configurations $T(\mathbf{x})$.

For the 2D quantum spin Hall surface states, it is the emergence of a WZW action, weighted by a $\mathbb{Z}_2$ topological angle in the effective low-energy description, that allows for topological metallic phases. The involved maps in momentum and real space read

$$U_{\mathbf{k}}: \mathbb{T}^2 \mapsto \text{U}(2)/\text{Sp}(2), \tag{32}$$

$$Q(\mathbf{x}): \mathbb{T}^2 \mapsto \text{O}(4R)/[\text{O}(2R) \times \text{O}(2R)], \tag{33}$$

with nontrivial homotopy groups, $\pi_2(\text{U}(2)/\text{Sp}(2)) = \mathbb{Z}_2$ and $\pi_2(\text{O}(4R)/[\text{O}(2R) \times \text{O}(2R)]) = \mathbb{Z}_2$, respectively. Both maps are thus characterized by nontrivial $\mathbb{Z}_2$ indices, and we already introduced a topological $\mathbb{Z}_2$ invariant for the Floquet operator (32) in Eq. (22). Alternatively, one can express the $\mathbb{Z}_2$ index as "half" of a Wess-Zumino-Witten term, which is readily extended to Eq. (33); see also Supplemental Material [29] for more details.

We conclude by remarking that the above discussion only relies on general structures, such as the soft-mode manifold identified in the course of the construction of the effective field theory, and it applies as a matter of principle. Whether there exist physical systems characterized by nontrivial couplings is an independent issue. The models we propose in the earlier sections are one option for how to realize nontrivial mappings utilizing the idea of engineered synthetic dimensions. In other words, in the present work, we provide the field theories, physical models, and numerical confirmation of topological Floquet metals for both complex and real symmetry classes, which are characterized by $\mathbb{Z}$ and $\mathbb{Z}_2$ topological indices, respectively. The presented structures encompass topological Floquet metal in other dimensions and symmetry classes.

VI. DISCUSSION

In this paper, we have introduced quantum simulators for topological surface states in isolation. Our proposal sidesteps the bulk-boundary principle and overcomes the fermion-doubling theorem, impeding the realization of isolated surface states in generic solid-state (lattice)

systems. The key element of our proposal is the dynamical generation of physical dimensions via external driving, using incommensurate frequencies. The simulation of extra dimensions via driving physical platforms has already been used in cold atom systems to measure the Anderson localization-delocalization transition in three dimensions to a degree of resolution not reachable in solid-state materials. Here, we have applied the idea to one-dimensional quantum walks of a spin-1/2 particle with time-dependent spin-rotation matrices, viz. "coin operations," following multifrequency dynamical protocols. The latter provide a flexibility absent in lattice systems, which allows for the simulation of (gauge) equivalent real-space dynamics involving long-range hopping.

We have illustrated the general idea with two specific examples: the three-dimensional topological surface states of a four-dimensional quantum Hall insulator and the two-dimensional surface states of a three-dimensional spin quantum Hall insulator. An inherent feature of both protocols is that the artificial generation of "synthetic" dimensions induces diffusive dynamics in all (gauge) equivalent space directions after a few iterations of the protocol, as verified in numerical simulations. Thus, our approach simulates the surfaces of "disordered" phases lacking translational invariance, which adds an element of realism. For both examples, we identified topological invariants showing the nontrivial topological nature of the dynamical protocols. Comparing simulations of the latter to those of topologically trivial parents with variable disorder strengths (respectively, bandwidth) clearly shows the impact of a nontrivial topology. While strong disorder turns the simulators of trivial metals into Anderson insulators, no signature of localization is found for the topological nontrivial protocols for all disorder strengths, respectively, bandwidths. Importantly, the numerical simulations show differences in the dynamics simulated by the different protocols after an experimentally accessible number of around $\mathcal{O}(20)$ time steps. This also sets the precision to which frequencies have to be chosen in experiment. Approximating irrational numbers by rational ones generates *finite* rather than infinitely extended synthetic dimensions. As long as the corresponding diffusion time (i.e., the time required to explore the finite dimension) exceeds the timescales probed in experiment, protocols with rational numbers can be used for all practical purposes.

Employing field-theory methods, we have shown that the quantum simulators generate dynamics within the same universality class as the corresponding topological insulator surface states. Specifically, we demonstrated that the universal long-time dynamics of the dynamical protocol is described by precisely the same topological field theory proposed for the simulated surface states. The field-theory construction builds on the color-flavor transformation and can be readily generalized to other symmetry classes and dimensions. Generalizing, e.g., the simulator of topological quantum Hall surface states to other (odd) dimensions, different from three, one can derive the corresponding Chern-Simons actions. Similarly, a topological field theory with Chern-Simons actions can be derived for the simulator probing the surface states of a quantum spin Hall insulator (class AII) in four dimensions and different from the $\mathbb{Z}_2$ field theory in three dimensions discussed here in detail. An exception is provided by class-AIII systems. These cannot be simulated within the proposed scheme since the gauge transformation, establishing the equivalence between the periodically driven and higher-dimensional systems, breaks chiral symmetry.

Our proposal required full dynamical control over a two-state internal degree of freedom ("spin"), which, at the current state, may be difficult to achieve in optical lattices. Therefore, we focused on the alternative platform of linear optical networks, similar to that used in Ref. [8]. Specifically, time-multiplexing networks with fast switching electro-optic modulators seem promising candidates for the implementation of the quantum simulators. We provided detailed blueprints for the experimental implementation of the two protocols within existing setups, realizing the quantum simulators of the surface states of a four-dimensional quantum Hall insulator and a three-dimensional quantum spin Hall insulator. We have shown in our numerical simulations that the experimental signature, viz. absence of Anderson localization, is observable within the experimentally realizable number of time steps. A tunable quantum simulator of topological surface states in isolation would open fascinating experimental possibilities. Specifically, it would provide a new, direct window into the intriguing physics resulting from the interplay of disorder and nontrivial topology.

ACKNOWLEDGMENTS

T. M. acknowledges financial support from Brazilian agencies CNPq and FAPERJ. K. W. K. acknowledges financial support from the Basic Science Research Program through the National Research Foundation of Korea (NRF) funded by the Ministry of Education (No. 2021R1F1A1055797) and the Korean Government (MSIT) (No. 2020R1A5A1016518). A. A. and D. B. were funded by the Deutsche Forschungsgemeinschaft (DFG) Projektnummer 277101999 TRR 183 (project A01/A02).

APPENDIX A: UNITARITY OF QUANTUM-WALK OPERATOR

The general, single time-step operator in Eq. (1) simplifies to Eq. (2) when focusing on quantum walks with short-range hopping $m = \{-1, 0, +1\}$. In the momentum representation,

$$\hat{U}_{\mathbf{k}} = \sum_{m=0,\pm} (\vec{r}_m \cdot \vec{\sigma}) e^{imk_1} = [\vec{r}_0 + (\vec{r}_+ + \vec{r}_-)\cos k_1 + i(\vec{r}_+ - \vec{r}_-)\sin k_1] \cdot \vec{\sigma}, \quad \text{(A1)}$$

where $\vec{r}_m$ is a four-component vector and $\vec{\sigma} = (\sigma_0, i\boldsymbol{\sigma})$. To satisfy unitarity, the vector multiplying $\vec{\sigma}$ must be real valued; that is, $\vec{r}_+ = (\vec{r}_-)^*$. Expressing $\vec{r}_+ = (\vec{r}_r + i\vec{r}_i)$ in terms of two real vectors $\vec{r}_r$, $\vec{r}_i$,

$$\hat{U}_{\mathbf{k}} = [\vec{r}_0 + (\vec{r}_r + i\vec{r}_i)e^{ik_1} + (\vec{r}_r - i\vec{r}_i)e^{-ik_1}] \cdot \vec{\sigma}, \quad \text{(A2)}$$

and requiring further that $\hat{U}_{\mathbf{k}}\hat{U}_{\mathbf{k}}^\dagger = \mathbb{1}$, the following relations can be verified:

$$\begin{aligned} &|\vec{r}_0|^2 + |\vec{r}_-|^2 + |\vec{r}_+|^2 = 1, \\ &|\vec{r}_0|^2 + 2|\vec{r}_r|^2 + 2|\vec{r}_i|^2 = 1, \\ &\vec{r}_r \cdot \vec{r}_i = 0, \vec{r}_r \cdot \vec{r}_0 = 0, \vec{r}_i \cdot \vec{r}_0 = 0, \\ &|\vec{r}_r| = |\vec{r}_i| = \frac{1}{2}\sqrt{1 - |\vec{r}_0|^2}. \end{aligned} \quad \text{(A3)}$$

These relations are stated below Eq. (2) in the main text.

APPENDIX B: SPREADING OF A WAVE PACKET

In this appendix, we demonstrate the equivalence of Eqs. (7) and (8). To this end, we introduce the initial density matrix

$$\rho_0 = \frac{1}{N_{\text{syn}}}\sum_{k_{\text{syn}},\sigma} |0, k_{\text{syn}}, \sigma\rangle\langle 0, k_{\text{syn}}, \sigma|, \qquad \rho_0^2 = \rho_0 \quad \text{(B1)}$$

(here, $n_1 = 0$ refers to the origin in the physical space and $N_{\text{syn}} \gg 1$ is the number of initial phases) and note that Eq. (7) for ΔX^2 can be cast in the basis-independent form

$$\langle \Delta X^2 \rangle = \text{tr}\overline{(\hat{\rho}_0 \mathcal{U}_{t,0}^\dagger \hat{n}_1^2 \mathcal{U}_{t,0})}, \quad \text{(B2)}$$

where $\overline{(\ldots)}$ refers to a disorder average. The rationale behind this expression is the following. The average over initial phases (momenta k_{syn}) implies the trace operation in the extended Hilbert space, and we discretize the corresponding momentum integral so that it becomes a sum over N_{syn} terms.

Further applying the time-dependent gauge transformation introduced in Sec. II A, one writes

$$\mathcal{U}_{t,0} = e^{it\sum_{j\geq 2}\omega_j \hat{n}_j}\mathcal{U}_F^t, \quad \text{(B3)}$$

where the Floquet operator $\mathcal{U}_F$ was defined in Eq. (6). This ansatz gives us the equivalent expression for the width of a wave packet,

$$\langle \Delta X^2 \rangle = \text{tr}(\hat{\rho}_0 (\mathcal{U}_F^\dagger)^t \hat{n}_1^2 \mathcal{U}_F^t). \quad \text{(B4)}$$

Lastly, to evaluate the trace above, one can use a full coordinate representation, which gives us

$$\langle \Delta X^2 \rangle = \frac{1}{N_{\text{syn}}}\sum_{\mathbf{n}\mathbf{n}',\sigma\sigma'} n_1^2 \overline{|\langle \mathbf{n}', \sigma'|\mathcal{U}_F^t|\mathbf{n}, \sigma\rangle|^2}, \quad \text{(B5)}$$

with $|\mathbf{n}, \sigma\rangle \equiv |n_1, n_{\text{syn}}, \sigma\rangle$ and $|\mathbf{n}', \sigma\rangle \equiv |n_1, n'_{\text{syn}}, \sigma'\rangle$. We then notice that upon a disorder average, the transition probability depends only on the difference in position, $\mathbf{n}' - \mathbf{n}$, and thereby, the expression (8) in the main text is recovered.

APPENDIX C: BLUEPRINT FOR THE $\text{FM}_{1+1_{\text{syn}}}$ SIMULATOR

A detailed blueprint for the optical linear network simulating the topological $\text{FM}_{1+1_{\text{syn}}}$ is shown in Fig. 7. The dynamical protocol, Eq. (20), involving all three components $\hat{R}_{\pm,0}$ requires a more complex setup in comparison to $\text{FM}_{1+2_{\text{syn}}}$ in class A, which now has to be built from two chiral half-step and two coin operations. Therefore, we start by summarizing the optical scheme in Fig. 7 and then provide its justification. To this end, we decompose the translational-invariant part of the single time-step evolution operator, Eq. (20), into the product

$$\mathcal{U}_{t+1,t} = \hat{U}_{\text{dis}}\hat{R}_a(t)\hat{T}_{\mathcal{C}}^{\frac{1}{2}}R_b(t)\hat{T}_{\mathcal{C}}^{\frac{1}{2}}, \quad \text{(C1)}$$

of a chiral half-step $\hat{T}_{\mathcal{C}}^{\frac{1}{2}}$ and coin operators $\hat{R}_{a/b}$. (The former are positioned in the four horizontal arms; notice the half fiber lengths $\tau_H/2$ and $\tau_V/2$, and the latter are placed in the vertical arms.) Dynamical EOMs after fiber lines of the first step operation allow us to terminate the walk by sending the photons to the detection unit. The coin operators are chosen as

$$\hat{R}_b(t) = YR_z(-\varphi_{2,t})Y^\dagger \equiv R_y(\varphi_{2,t}), \quad \text{(C2)}$$

where $Y = e^{i\pi\sigma_1/4}$ is the matrix of y-basis change [25], and $\hat{R}_a(t) = \hat{R}_{a,t+1}^{(\text{II})}\hat{R}_{a,t}^{(\text{I})}$, with

$$\hat{R}_{a,t}^{(\text{I})} = \begin{cases} R_z(\varphi_{2,t})\hat{Y}^\dagger & \sin\varphi_{2,t} \geq 0 \\ \hat{Y}^\dagger & \sin\varphi_{2,t} < 0 \end{cases} \quad \text{(C3)}$$

and

$$\hat{R}_{a,t+1}^{(\text{II})} = \begin{cases} \hat{Y} & \sin\varphi_{2,t+1} \geq 0 \\ \hat{Y}R_z(\varphi_{2,t+1}) & \sin\varphi_{2,t+1} < 0 \end{cases} \quad \text{(C4)}$$

with $\varphi_{2,t} = k_2 + \omega_2 t$. Finally, disorder is introduced by placing the local, time-reversal-invariant random potential $U(n_1) = e^{i\phi_{n_1}\sigma_0}$ in between $R_{a,t}^{(\text{I})}$ and $R_{a,t+1}^{(\text{II})}$, with position-dependent angles ϕ_{n_1}, randomly drawn from the unit circle $-\pi \leq \phi_{n_1} < \pi$.

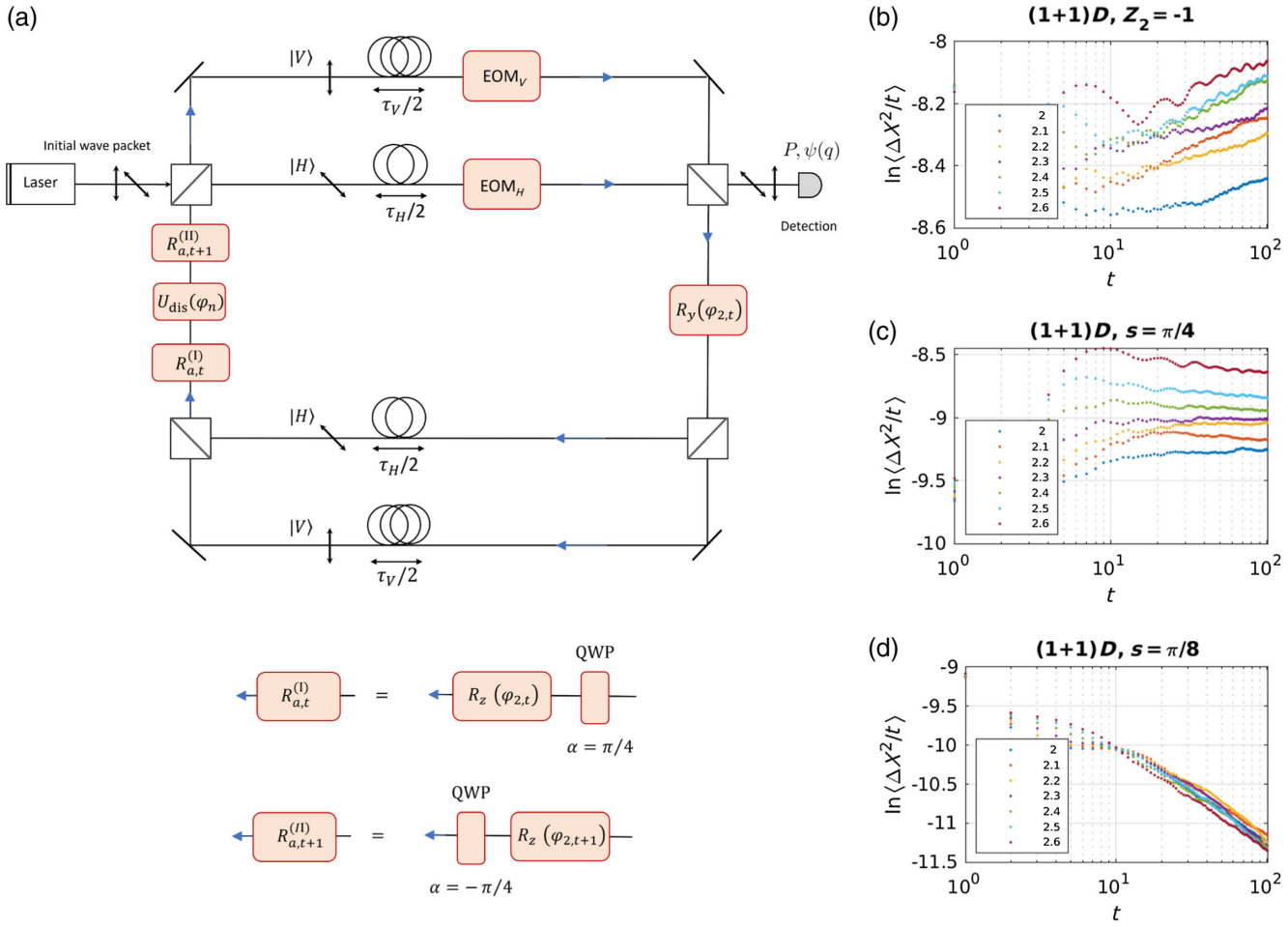

FIG. 7. Blueprint of an optical linear network simulating the topological surface states of a 3D quantum spin Hall insulator in the quantum-walk setting. (a) Feedback loop built from the step operator $\hat{T}_C^{\pm\frac{1}{2}}$ (upper and middle arms, respectively) and the coin operators $\hat{R}_a$ and $\hat{R}_b$ (right and left arms, respectively); for details, see main text. To the left and right of the loop, source and detection units are connected. (b) Numerical simulation of a topological metal ($\mathbb{Z}_2 = -1$) in a $(1 + 1_{\rm syn})D$ quantum walk for short time steps accessible by experiments. The width of the wave packet scaled by time is plotted on a log scale, showing that diffusion is anomalously fast. (c) Critical quantum walk in $(1 + 1_{\rm syn})D$ class A at a topological quantum phase transition, showing the same scaling with the classical diffusion $\langle\Delta X^2\rangle \sim t$. (d) Quantum walk in $(1 + 1_{\rm syn})D$ class A without a topological term, showing Anderson localization. Colors correspond to incommensurate frequencies $\omega_2 = \sqrt{5}C$ with values for C as indicated in the legends.

Coming back to the justification of Eq. (C1), we note that expressing the time-evolution operator in Eq. (20) as the product of elementary chiral translations and coin operators is not immediately straightforward. We first notice that upon replacing $|\sin k_2| \to \sin k_2$ in Eq. (21), the model is reduced to the familiar 2D class-A Floquet insulator [28,41], which is built by the multiplication of simpler operators. For an implementation of the protocol with absolute value $|\sin k_2|$, we separate cases $\sin k_2 \le 0$ and $\sin k_2 > 0$. Specifically, a class-A 2D Floquet model with homotopy parameter s [28] is written as the product of four unitary operators $\hat{U}_{\rm A} = \hat{U}_4\hat{U}_3\hat{U}_2\hat{U}_1$, with

$$\hat{U}_i(k) = \cos(s) + i\sin(s)\begin{pmatrix} & e^{-i\mathbf{k}\cdot\mathbf{v}_i} \\ e^{i\mathbf{k}\cdot\mathbf{v}_i} & \end{pmatrix}.$$

Here, $(\mathbf{v}_1, \mathbf{v}_2, \mathbf{v}_3, \mathbf{v}_4) = (0, -\mathbf{e}_1, -\mathbf{e}_1 + \mathbf{e}_2, \mathbf{e}_2)$, with $\mathbf{e}_{1,2}$ lattice unit vectors in the horizontal or vertical direction. At $s = \pi/4$, the product of unitaries can be expanded in the quantum-walk form,

$$\hat{U}_{\rm A} = (\hat{r}_0 \cdot \vec{\sigma}) + (\vec{r}_+ \cdot \vec{\sigma})e^{ik_1} + (\vec{r}_- \cdot \vec{\sigma})e^{-ik_1},$$

where

$$\vec{r}_0 = \frac{1}{2}(1 - \cos k_2, 0, 0, \sin k_2),$$
$$\vec{r}_r = \frac{1}{4}(-1 - \cos k_2, 0, 0, \sin k_2),$$
$$\vec{r}_i = \frac{1}{4}(0, \sin k_2, -1 - \cos k_2, 0).$$

Following the general recipe outlined in Sec. II A, we simulate the 2D dynamics as a 1D quantum walk with a time-dependent protocol, replacing momentum $k_2 \to \varphi_{2,t}$ by a time-dependent angle. We then notice that for $\sin\varphi_{2,t} > 0$, vectors $\vec{r}_{0,r,i}$ of $\hat{U}_{\rm A}$ are identical to those of $\hat{U}_{\rm AII}$ in Eq. (20). Hence, when $\sin\varphi_{2,t} > 0$, the quantum-walk operator in Eq. (20) can be written as the product of the four unitary operators, $\hat{U}_{\rm AII}(\sin\varphi_{2,t} > 0) = \hat{U}_{\rm A}(k_1, \varphi_{2,t})$. When $\sin\varphi_{2,t} < 0$, on the other hand, one can verify that $\hat{U}_{{\rm AII},\sin\varphi_{2,t}<0}(k_1, \varphi_{2,t}) = \hat{U}_{\rm A}^T(-k_1, \varphi_{2,t}, s = (\pi/4))$.

Next, we express $\hat{U}_{j=1,2,3,4}$ as a combination of shift and rotation operators,

$$\begin{aligned}
\hat{U}_1 &= e^{is\sigma_1},\\
\hat{U}_2 &= \hat{T}_C^{-\frac{1}{2}} e^{is\sigma_1} \hat{T}_C^{\frac{1}{2}},\\
\hat{U}_3 &= e^{i\varphi_{2,t}\sigma_3/2} \hat{T}_C^{-\frac{1}{2}} e^{is\sigma_1} \hat{T}_C^{\frac{1}{2}} e^{-i\varphi_{2,t}\sigma_3/2},\\
\hat{U}_4 &= e^{i\varphi_{2,t}\sigma_3/2} e^{is\sigma_1} e^{-i\varphi_{2,t}\sigma_3/2},
\end{aligned}$$

with the "half" translation operator $\hat{T}_C^{\frac{1}{2}} = e^{ik_1\sigma_3/2}$. We stress that the full Floquet operator $\hat{U}_{\rm A}$ is 2π periodic in k_1, and the appearance of a half translation operator does not imply a doubling of the unit cell. The same is true for the topological Floquet metal model.

The 2D class-AII model is expressed as

$$\begin{aligned}
&\hat{U}_{{\rm AII},\sin\varphi_{2,t}\geq 0}(k_1, \varphi_{2,t})\\
&\quad = \hat{U}_{\rm A}\left(k_1, \varphi_{2,t}, s = \frac{\pi}{4}\right)\\
&\quad = e^{i\varphi_{2,t}\sigma_3/2} Y \hat{T}_C^{-\frac{1}{2}} Y e^{-i\varphi_{2,t}\sigma_3/2} Y \hat{T}_C^{\frac{1}{2}} Y,\\
&\quad = -e^{i\varphi_{2,t}\sigma_3/2} Y^\dagger \hat{T}_C^{\frac{1}{2}} Y^\dagger e^{-i\varphi_{2,t}\sigma_3/2} Y \hat{T}_C^{\frac{1}{2}} Y, \qquad \text{(C5)}
\end{aligned}$$

and to arrive at this result, we used $Y\hat{T}_C^{-\frac{1}{2}}Y = -Y^\dagger \hat{T}_C^{\frac{1}{2}} Y^\dagger$ and commutativity of operators $\hat{T}_C^{\frac{1}{2}}$ and $e^{-i\varphi_{2,t}\sigma_3/2}$. On the other hand,

$$\begin{aligned}
&\hat{U}_{{\rm AII},\sin\varphi_{2,t}<0}(k_1, \varphi_{2,t})\\
&\quad = \hat{U}_{\rm A}^T\left(-k_1, \varphi_{2,t}, s = \frac{\pi}{4}\right)\\
&\quad = Y \hat{T}_C^{-\frac{1}{2}} Y e^{-i\varphi_{2,t}\sigma_3/2} Y \hat{T}_C^{\frac{1}{2}} Y e^{i\varphi_{2,t}\sigma_3/2}\\
&\quad = -Y^\dagger \hat{T}_C^{\frac{1}{2}} Y^\dagger e^{-i\varphi_{2,t}\sigma_3/2} Y \hat{T}_C^{\frac{1}{2}} Y e^{i\varphi_{2,t}\sigma_3/2}, \qquad \text{(C6)}
\end{aligned}$$

and from the relations (C5) and (C6), we notice that $\hat{U}_{\rm AII} = R_a^{(\rm I)} \hat{T}_C^{\frac{1}{2}} R_b \hat{T}_C^{\frac{1}{2}} R_a^{(\rm II)}$. Up to a cyclic permutation of the operator $R_a^{(\rm II)}$, this is equivalent to the clean part of $\mathcal{U}_{t+1,t}$; see Eq. (C1). Notice that in both cases, $\hat{U}_{\rm AII}$ involves the same unitary sandwiched between the two $\hat{T}_C^{\frac{1}{2}}$, which simplifies the implementation of $\hat{R}_b(t) = Y^\dagger e^{-i\varphi_{2,t}\sigma_3/2} Y$. On the other hand, $\hat{R}_a(t)$ depends on the sign of $\sin\varphi_{2,t}$.

APPENDIX D: $\mathbb{Z}_2$ TOPOLOGICAL INVARIANT

In this appendix, we further discuss the $\mathbb{Z}_2$ topological invariant for the two-band model and prove the relation (23). The unitary operator $\hat{U}_{\mathbf{k}}$ gives rise to the auxiliary Hamiltonian [3,42]

$$\tilde{H}_U(\mathbf{k}) = \begin{pmatrix} 0 & U_{\mathbf{k}} \\ U_{\mathbf{k}}^\dagger & 0 \end{pmatrix}, \qquad \text{(D1)}$$

which shares time-reversal and particle-hole symmetries, $\hat{\Theta}_1 \tilde{H}_U(\mathbf{k}) \hat{\Theta}_1^{-1} = \tilde{H}_U(-\mathbf{k})$ and $\hat{\Theta}_2 \tilde{H}_U(\mathbf{k}) \hat{\Theta}_2^{-1} = -\tilde{H}_U(-\mathbf{k})$, respectively, with $\hat{\Theta}_1 = \tau_1 \otimes i\sigma_2\mathcal{K}$ and $\hat{\Theta}_2 = i\tau_2 \otimes i\sigma_2\mathcal{K}$. In other words, H_U belongs to class DIII. Notice that in Eq. (D1), off-diagonal elements are the Floquet unitary operators without band flattening, allowing us to make a connection between the $\mathbb{Z}_2$ invariant and the eigenenergies at time-reversal-invariant momenta.

One way to compute the $\mathbb{Z}_2$ topological invariant is as follows [26]: The Hamiltonian has two valence bands at energy $E = -1$, and their eigenvectors are

$$u_1^-(\mathbf{k}) = \frac{1}{\sqrt{2}} \begin{pmatrix} -1 \\ 0 \\ U_{\mathbf{k},11}^* \\ U_{\mathbf{k},12}^* \end{pmatrix}, \quad u_2^-(\mathbf{k}) = \frac{1}{\sqrt{2}} \begin{pmatrix} 0 \\ -1 \\ U_{\mathbf{k},21}^* \\ U_{\mathbf{k},22}^* \end{pmatrix}, \qquad \text{(D2)}$$

where $U_{\mathbf{k},ij}^* = (U_{\mathbf{k}}^\dagger)_{ji}$. The sewing matrix, which is needed to compute the topological invariant [26], can be obtained from these two vectors as $(w_{\mathbf{k}})_{ab} = \langle u_a^-(-\mathbf{k}) | \hat{\Theta}_1 u_b^-(\mathbf{k}) \rangle$. In other words,

$$\begin{aligned}
w_{\mathbf{k}} &= \frac{1}{2} \begin{pmatrix} -U_{\mathbf{k},12} + U_{-\mathbf{k},12} & -U_{\mathbf{k},22} - U_{-\mathbf{k},11} \\ U_{\mathbf{k},11} + U_{-\mathbf{k},22} & U_{\mathbf{k},21} - U_{-\mathbf{k},21} \end{pmatrix} \qquad \text{(D3)}\\
&= \begin{pmatrix} -U_{\mathbf{k},12} & -U_{\mathbf{k},22} \\ U_{\mathbf{k},11} & U_{\mathbf{k},21} \end{pmatrix} \qquad \text{(D4)}\\
&= -i\sigma_2 U_{\mathbf{k}}^T, \qquad \text{(D5)}
\end{aligned}$$

where, in the second line, time-reversal symmetry of the unitary operator is used, i.e., $U_{\mathbf{k},11} = U_{-\mathbf{k},22}$, $U_{\mathbf{k},12} = -U_{-\mathbf{k},12}$ and $U_{\mathbf{k},21} = -U_{-\mathbf{k},21}$ (as follows from $\sigma_2 U_{\mathbf{k}} \sigma_2 = U_{-\mathbf{k}}^T$). One can then readily verify that the sewing matrix is antisymmetric at time-reversal-invariant momenta $\mathbf{\Lambda}_1 = (0,0)$, $\mathbf{\Lambda}_2 = (\pi, 0)$, $\mathbf{\Lambda}_3 = (0, \pi)$, and $\mathbf{\Lambda}_4 = (\pi, \pi)$, i.e.,

$$w_{\mathbf{\Lambda}_j} = \frac{1}{2}\begin{pmatrix} 0 & -U_{\mathbf{\Lambda}_j,11} - U_{\mathbf{\Lambda}_j,22} \\ U_{\mathbf{\Lambda}_j,11} + U_{\mathbf{\Lambda}_j,22} & 0 \end{pmatrix}, \quad \text{(D6)}$$

where $U_{\mathbf{\Lambda}_j,11} = U_{\mathbf{\Lambda}_j,22}$, and the Pfaffian is $\mathrm{Pf}[w_{\mathbf{\Lambda}_j}] = -\frac{1}{2}(U_{\mathbf{\Lambda}_j,11} + U_{\mathbf{\Lambda}_j,22}) = -\frac{1}{2}\mathrm{tr}[U_{\Lambda_j}] = -\exp(i\epsilon_{\mathbf{\Lambda}_j})$. Finally, the $\mathbb{Z}_2$ topological invariant becomes

$$W_{\mathbb{Z}_2} = \prod_{j=1,2,3,4} \mathrm{Pf}[w_{\mathbf{\Lambda}_j}] = \exp\left(i \sum_{j=1,2,3,4} \epsilon_{\Lambda_j}\right), \quad \text{(D7)}$$

which implies that the condition for a nontrivial Floquet topological metal, $W_{\mathbb{Z}_2} = -1$, translates into $\sum_{j=1,2,3,4} \epsilon_{\Lambda_j} = \pi \pmod{2\pi}$.

[1] B. Sbierski, J. F. Karcher, and M. S. Foster, *Spectrum-Wide Quantum Criticality at the Surface of Class AIII Topological Phases: An "Energy Stack" of Integer Quantum Hall Plateau Transitions*, Phys. Rev. X **10**, 021025 (2020).

[2] X.-Q. Sun, M. Xiao, T. c. v. Bzdušek, S.-C. Zhang, and S. Fan, *Three-Dimensional Chiral Lattice Fermion in Floquet Systems*, Phys. Rev. Lett. **121**, 196401 (2018).

[3] S. Higashikawa, M. Nakagawa, and M. Ueda, *Floquet Chiral Magnetic Effect*, Phys. Rev. Lett. **123**, 066403 (2019).

[4] J. Chabé, G. Lemarié, B. Grémaud, D. Delande, P. Szriftgiser, and J. C. Garreau, *Experimental Observation of the Anderson Metal-Insulator Transition with Atomic Matter Waves*, Phys. Rev. Lett. **101**, 255702 (2008).

[5] G. Lemarié, J. Chabé, P. Szriftgiser, J. C. Garreau, B. Grémaud, and D. Delande, *Observation of the Anderson Metal-Insulator Transition with Atomic Matter Waves: Theory and Experiment*, Phys. Rev. A **80**, 043626 (2009).

[6] A. Schreiber, A. Gábris, P. P. Rohde, K. Laiho, M. Štefaňák, V. Potoček, C. Hamilton, I. Jex, and C. Silberhorn, *A 2D Quantum Walk Simulation of Two-Particle Dynamics*, Science **336**, 55 (2012).

[7] L. Lorz, E. Meyer-Scott, T. Nitsche, V. Potoček, A. Gábris, S. Barkhofen, I. Jex, and C. Silberhorn, *Photonic Quantum Walks with Four-Dimensional Coins*, Phys. Rev. Res. **1**, 033036 (2019).

[8] A. Geraldi, S. De, A. Laneve, S. Barkhofen, J. Sperling, P. Mataloni, and C. Silberhorn, *Transient Subdiffusion via Disordered Quantum Walks*, Phys. Rev. Res. **3**, 023052 (2021).

[9] G. Casati, I. Guarneri, and D. L. Shepelyansky, *Anderson Transition in a One-Dimensional System with Three Incommensurate Frequencies*, Phys. Rev. Lett. **62**, 345 (1989).

[10] F. Haake, *Quantum Signatures of Chaos* (Springer-Verlag, Berlin, Heidelberg, 2006).

[11] D. L. Shepelyansky, *Localization of Quasienergy Eigenfunctions in Action Space*, Phys. Rev. Lett. **56**, 677 (1986).

[12] F. L. Moore, J. C. Robinson, C. Bharucha, P. E. Williams, and M. G. Raizen, *Observation of Dynamical Localization in Atomic Momentum Transfer: A New Testing Ground for Quantum Chaos*, Phys. Rev. Lett. **73**, 2974 (1994).

[13] C. Tian and A. Altland, *Theory of Localization and Resonance Phenomena in the Quantum Kicked Rotor*, New J. Phys. **12**, 043043 (2010).

[14] G. Lemarié, H. Lignier, D. Delande, P. Szriftgiser, and J. C. Garreau, *Critical State of the Anderson Transition: Between a Metal and an Insulator*, Phys. Rev. Lett. **105**, 090601 (2010).

[15] C. Tian, Y. Chen, and J. Wang, *Emergence of Integer Quantum Hall Effect from Chaos*, Phys. Rev. B **93**, 075403 (2016).

[16] I. Martin, G. Refael, and B. Halperin, *Topological Frequency Conversion in Strongly Driven Quantum Systems*, Phys. Rev. X **7**, 041008 (2017).

[17] E. J. Meier, F. A. An, A. Dauphin, M. Maffei, P. Massignan, T. L. Hughes, and B. Gadway, *Observation of the Topological Anderson Insulator in Disordered Atomic Wires*, Science **362**, 929 (2018).

[18] A. Schreiber, K. N. Cassemiro, V. Potoček, A. Gábris, P. J. Mosley, E. Andersson, I. Jex, and C. Silberhorn, *Photons Walking the Line: A Quantum Walk with Adjustable Coin Operations*, Phys. Rev. Lett. **104**, 050502 (2010).

[19] J. P. Dahlhaus, J. M. Edge, J. Tworzydło, and C. W. J. Beenakker, *Quantum Hall Effect in a One-Dimensional Dynamical System*, Phys. Rev. B **84**, 115133 (2011).

[20] J. M. Edge, J. Tworzydło, and C. W. J. Beenakker, *Metallic Phase of the Quantum Hall Effect in Four-Dimensional Space*, Phys. Rev. Lett. **109**, 135701 (2012).

[21] C. Tian, Y. Chen, and J. Wang, *Emergence of Integer Quantum Hall Effect from Chaos*, Phys. Rev. B **93**, 075403 (2016).

[22] I. Petrides, H. M. Price, and O. Zilberberg, *Six-Dimensional Quantum Hall Effect and Three-Dimensional Topological Pumps*, Phys. Rev. B **98**, 125431 (2018).

[23] For $n \neq \pm 1$, $\int_{-\pi}^{\pi} e^{ik_2 n} |\sin k_2| dk_2 = (2/n^2 - 1)((-1)^{n+1} - 1)$.

[24] M. S. Rudner, N. H. Lindner, E. Berg, and M. Levin, *Anomalous Edge States and the Bulk-Edge Correspondence for Periodically Driven Two-Dimensional Systems*, Phys. Rev. X **3**, 031005 (2013).

[25] For example, rotation around the y axis, $\hat{R}_2(\varphi) = e^{i\pi\sigma_1/4}\hat{R}_3(\varphi)e^{-i\pi\sigma_1/4}$, is implemented using the quarter-wave plates aligned at an angle $\pi/4$, $\hat{C}_{\mathrm{QWP}}(\pi/4) = e^{-i\pi\sigma_1/4}$ [8], while the rotation around the x axis, $\hat{R}_1(\varphi) = e^{-i\pi\sigma_2/4}\hat{R}_3(\varphi)e^{i\pi\sigma_2/4}$, is implemented by using the two half wave plates: $\hat{C}_{\mathrm{HWP}}(\pi/8)\hat{C}_{\mathrm{HWP}}(0) = e^{-i\pi\sigma_2/4}$ [18].

[26] S. Ryu, A. P. Schnyder, A. Furusaki, and A. W. W. Ludwig, *Topological Insulators and Superconductors: Tenfold Way and Dimensional Hierarchy*, New J. Phys. **12**, 065010 (2010).

[27] C. Tian, *Anomalous Quantum Diffusion and the Topological Metal*, Phys. Rev. B **86**, 121304(R) (2012).

[28] K. W. Kim, D. Bagrets, T. Micklitz, and A. Altland, *Quantum Hall Criticality in Floquet Topological Insulators*, Phys. Rev. B **101**, 165401 (2020).

[29] See Supplemental Material at http://link.aps.org/supplemental/10.1103/PhysRevX.13.011003 for the effective field theory description of the quantum simulator protocols.

[30] F. Wegner, *The Mobility Edge Problem: Continuous Symmetry and a Conjecture*, Z. Phys. B **35**, 207 (1979).

[31] K. B. Efetov, A. I. Larkin, and D. E. Khmel'nitskii, *Interaction of Diffusion Modes in the Theory of Localization*, JETP **52**, 568 (1980).

[32] A. M. Pruisken and L. Schäfer, *The Anderson Model for Electron Localisation Non-linear σ Model, Asymptotic Gauge Invariance*, Nucl. Phys. **B200**, 20 (1982).
[33] K. B. Efetov and A. I. Larkin, *Kinetics of a Quantum Particle in Long Metallic Wires*, Sov. Phys. JETP **58**, 444 (1983).
[34] A. Pruisken, *On Localization in the Theory of the Quantized Hall Effect: A Two-Dimensional Realization of the θ-Vacuum*, Nucl. Phys. **B235**, 277 (1984).
[35] K. B. Efetov, *Supersymmetry in Disorder and Chaos* (Cambridge University Press, Cambridge, England, 1997).
[36] A. Altland and D. Bagrets, *Theory of the Strongly Disordered Weyl Semimetal*, Phys. Rev. B **93**, 075113 (2016).
[37] Y. X. Zhao and Z. D. Wang, *General Response Theory of Topologically Stable Fermi Points and Its Implications for Disordered Cases*, Phys. Rev. B **92**, 085143 (2015).
[38] S. Ryu, C. Mudry, H. Obuse, and A. Furusaki, *$\mathbb{Z}_2$ Topological Term, the Global Anomaly, and the Two-Dimensional Symplectic Symmetry Class of Anderson Localization*, Phys. Rev. Lett. **99**, 116601 (2007).
[39] E. J. König, P. M. Ostrovsky, I. V. Protopopov, I. V. Gornyi, I. S. Burmistrov, and A. D. Mirlin, *Interaction and Disorder Effects in Three-Dimensional Topological Insulator Thin Films*, Phys. Rev. B **88**, 035106 (2013).
[40] P. M. Ostrovsky, I. V. Gornyi, and A. D. Mirlin, *Quantum Criticality and Minimal Conductivity in Graphene with Long-Range Disorder*, Phys. Rev. Lett. **98**, 256801 (2007).
[41] M. S. Rudner, N. H. Lindner, E. Berg, and M. Levin, *Anomalous Edge States and the Bulk-Edge Correspondence for Periodically Driven Two-Dimensional Systems*, Phys. Rev. X **3**, 031005 (2013).
[42] R. Roy and F. Harper, *Periodic Table for Floquet Topological Insulators*, Phys. Rev. B **96**, 155118 (2017).